Journal of Cleaner Production 233 (2019) 972–992

Contents lists available at ScienceDirect

Journal of Cleaner Production

journal homepage: www.elsevier.com/locate/jclepro

Investigating urban heat island through spatial analysis of New York City streetscapes

Richard R. Shaker [a, b, c, *], Yaron Altman [d], Chengbin Deng [d], Eric Vaz [a, b, c], K.Wayne Forsythe [a, b, c]

[a] Department of Geography & Environmental Studies, Ryerson University, Toronto, Ontario, Canada
[b] Graduate Programs in Environmental Applied Science & Management, Ryerson University, Toronto, Ontario, Canada
[c] Graduate Program in Spatial Analysis, Ryerson University, Toronto, Ontario, Canada
[d] Department of Geography, Binghamton University, State University of New York, Binghamton, NY 13902, USA

ARTICLE INFO

Article history:
Received 23 July 2018
Received in revised form
21 December 2018
Accepted 31 May 2019
Available online 14 June 2019

Handling Editor: Mingzhou Jin

Keywords:
Geographically weighted regression
Landscape configuration
Streetscapes
Sustainable urbanization
Urban landscape
Urban heat island

ABSTRACT

Cities experience the urban heat island (UHI), which continue to pose challenges for humanity's increasingly urban population. Past research has revealed that land cover composition and configuration, along with other geographical phenomena (i.e., albedo), can explain much of the spatial pattern of UHI, yet advances await. In response, this research was made to: (*i*) assess the spatial pattern of mean ambient night temperature across 34 streetscapes in New York City (NYC); (*ii*) create and differentiate global and local regression models between-natural and built streetscape characteristics- and mean ambient night temperature; and (*iii*) use geographically weighted regression (GWR) to assess local patterns of correlated associations. Urban canopy layer (UCL) temperatures were recorded across 34 weather stations, and landscape metrics calculated from 0.914 m land cover data with 96% accuracy. Local Getis-Ord Gi* statistic exhibited significant spatial cold and hot spots of UHI in NYC. Global inferential tests revealed that sky-view factor, photosynthesis activity, elevation, and road configuration were the strongest predictors of mean ambient night temperature. Six multiple regression models were ultimately made with GWR fitting the UHI aptly ($R^2 = 65–74\%$). Important explanatory covariates were illustrated using local pseudo-*t* statistics and linked to mean ambient night temperature, supporting the importance of GWR for understanding local UHI interactions. Results also confirm that landscape configuration metrics are stronger predictors of UHI than composition measures. Streetscape design, particularly road patterns and process, requires more consideration when attempting to mitigate UHI during future sustainability planning, urban renewal projects, and research.

1. Introduction

Population growth and rural-to-urban migration continue to fill already swollen cities. Due to technological advances during the Industrial Revolution, high birth rates and low death rates that followed, global human population continues to be positive and strong (Wu, 2008). According to the United Nations Population Division (2014), global urban population will increase by an extra 2.5 billion between 2010 and 2050. Recently, global population was estimated to reach somewhere between 9.6 and 12.3 billion by 2100 and increase thereafter with an unknown stabilization date (Gerland et al., 2014). In 2008, a landmark was reached in human evolution with over half of humanity living in cities; furthermore, the number of megacities (populations over 10 million) increased from 3 in 1975 to 19 in 2007, and was anticipated to expand to 27 by 2025 (Crane and Kinzig, 2005; UNPD, 2008). The developing world continues to absorb the majority of rural to urban migration; the developed world has approached urban population saturation with more than 80% already living in cities (UNPD, 2014). A few countries have already reached the milestone of 100% urban population, and it has been fathomed that almost all of humanity could live in an urban setting by the next century. In a prediction by Batty (2011), global population was estimated to be 70% urban by 2050 and 100% urban by 2092. Although urbanization is often correlated with improved socioeconomic well-being, it has been simultaneously

* Corresponding author. Ryerson University, Toronto, Ontario, Canada.
E-mail addresses: rshaker@ryerson.ca (R.R. Shaker), yaltman2@binghamton.edu (Y. Altman), cdeng@binghamton.edu (C. Deng), vaz@ryerson.ca (E. Vaz), forsythe@ryerson.ca (K.Wayne Forsythe).

https://doi.org/10.1016/j.jclepro.2019.05.389
0959-6526/

linked to environmental problems that degrade Earth's life-supporting systems (Shaker, 2015). Besides direct impacts, urbanization metabolizes biogeochemical resources and disturbs life-supporting ecosystems great distances from epicenters (Alberti, 2008; Carpenter et al., 2009; Weinzettel et al., 2013; Turner and Gardner, 2015). Consequently, urbanization is likely having the greatest direct and indirect influence on global change (Foley et al., 2005; Liu et al., 2007; Grimm et al., 2008; Rockström et al., 2009; Pickett et al., 2011; Shaker, 2015; Forman and Wu, 2016; Ceballos et al., 2017).

Urban heat island (UHI) is the most recognizable example of human-induced climate alteration. A phenomenon recognized since the early 1800s (Yang et al., 2015), but not coined until the 1940s (Balchin and Pye, 1947), UHI is the term used to depict hotter surface and atmospheric temperatures found in urban areas compared to their cooler suburban, exurban, and rural counterparts (Oke, 1982, 1988; Voogt and Oke, 2003). Specifically, increased urban temperatures exist because: built-up places have increased human-created heat; accommodation of solar radiation into urban structures; scarcity of cool sinks such as lakes and forests; stagnant air due to city structures; and greenhouse gases (GHG) not allowing long-wave radiation to escape back to space (Oke, 2002). With impacts to socioeconomic and environmental well-being, UHI has garnered much attention from environmental and sustainability scientists, urban and regional planners, and public health officials. With urban expansion eminent (Batty, 2008, 2011; Seto et al., 2012), city energy use, anthropogenic GHG, and other air pollutants will increase under foreseeable population growth, rural to urban migration, technology and consumption trends. According to Seto et al. (2014), urban areas consume 67–76% of global energy and are guilty for releasing 71–76% of fossil fuel-related CO_2. UHI increase consumption of cooling energy (Santamouris et al., 2015), which surges energy demand on power plants, ultimately increasing production of GHG that accelerate global warming (Akbari et al., 2001; Kolokotroni et al., 2007). These energy surges in cities have also been linked to increased concentrations of ground-level ozone (Akbari et al., 2001; Stathopoulou et al., 2008), particulate matter (Parrish and Zhu, 2009), and other regional atmospheric pollution (Sarrat et al., 2006; Schweitzer and Zhou, 2010). Residential water use and associated utility costs also increase substantially when urban temperatures rise (Guhathakurta and Gober, 2007). Evidence supports that morbidity and mortality are exacerbated in locations impacted by UHI (Norton et al., 2015), which are anticipated to worsen with climate change (Stone, 2012). Specifically, mortality risk for nursing home residents (Klenk et al., 2010), infant stress, and sudden infant death syndrome incidents (Scheers-Masters et al., 2004) increase with severe heat occurrences in cities. Lastly, thermal comfort levels deteriorate in both outdoor and indoor environments during elevated heat events (Pantavou et al., 2011; de Abreu-Harbich et al., 2015), contributing to heat wave disasters (Duneier, 2006; Klinenberg, 2015).

Engineering, architecture, urban planning and design, along with a multitude of research and professional fields, continue to develop technology and strategies for remediating the UHI. The main mitigation goal is to reach thermal equilibrium by decreasing heating and increasing corresponding cooling in urban areas (Santamouris, 2014). In doing so, new temperature reducing technology have been created and implemented primarily at the building scale, with other advancements at street and landscape scales. Specific to buildings, increasing rooftop albedo through use of reflective or white materials (Synnefa et al., 2008; Yang et al., 2015) and growing native vegetation (Bowler et al., 2010; Berardi et al., 2014) has effectively lowered urban ambient temperatures by decreasing sensible heat flux. Reflective coatings on external walls also increase building albedo (Karlessi et al., 2009), and various insulating materials have decreased cooling energy needs (Jim, 2014). At the street and landscape scales, most urban cooling improvements have also focused on albedo, but have expanded to include natural and human-made heat sinks (Bowler et al., 2010; Coutts et al., 2013). A major strategy for cities is to enhance human and ecological well-being by enlarging existing green spaces, building new green infrastructure, restoring historic or creating new heat sinks. Specifically, natural heat sinks can be enhanced through connecting existing parks by riparian corridors, creating artistic water features, enhancing tree shading, building greenways, and implementing best management practices such as rain gardens, bioretention basins, and restoring wetlands (Akbari et al., 2001; Gill et al., 2007; Coutts et al., 2013; Jim et al., 2015; Yang et al., 2015). Additional advances have been proposed and created to mitigate UHI phenomenon using cool pavements. According to a review by Santamouris (2013), reflective, permeable and water absorbent pavements have the capacity to decrease temperatures considerably within urban settings. Despite the aforementioned technological advancements, no agreement exists on how best to mitigate or eliminate UHI occurrence or associated impacts.

The structure of urban density and geometry influence surface radiation processes, which in turn alters local and regional climate (Wu, 2008). According to Stewart and Oke (2012), these climate zone variations are linked to: *i*) built-up geometry (e.g., building height to street width ratio); *ii*) land cover (e.g., composition of urban vs. forested); *iii*) urban materials (e.g., glass vs. concrete vs. steel); *iv*) energy metabolism (e.g., cooling waste energy). Due to the coupling of urban *streetscapes* and urban climate processes, researchers have previously employed landscape ecology metrics for understanding UHI patterns and statistically supporting restorative urban design strategies (e.g., Li et al., 2011; Zhou et al., 2011; Connors et al., 2013; Kong et al., 2014; Zhou et al., 2017; Greene and Kedron, 2018). Landscape ecology emphases two major components of landscape: *i*) structure, or the spatial configuration of its elements (i.e., land cover patch shape); and *ii*) function, or the biogeophysical processes (i.e., long-wave radiation) that modify or result from its configuration (Tischendorf and Fahrig, 2000). Despite an established research history between landscape and urban ambient temperature, studies have rendered inconclusive evidence if it is land cover configuration or composition that is more important at explaining UHI (Zhou et al., 2011, 2017; Li et al., 2013; Connors et al., 2013). Previous findings suggest that proportions of land cover can explain much (but by no means all) of the variability in urban ambient air temperature; however, composition measures lack the detailed design information required for creating resilient landscapes and sustainable cities. Another gap within recent UHI literature is the primary reliance on remotely sensed land surface temperature (LST) for investigating inference between landscapes and UHI (e.g., Buyantuyev and Wu, 2010; Zhou et al., 2011; Deng and Wu, 2013; Zhou et al., 2014; Jenerette et al., 2016; Zhou et al., 2017; Greene and Kedron, 2018). Although there are many benefits for using these data, such as rapidly evaluating vast geographic regions, pixel size (resolution) and validation limitations remain, and often advanced remote sensing skills are required (Myint et al., 2013; Song et al., 2014; Jenerette et al., 2016). Lastly, although Zhou et al. (2017) recently suggested spatial autocorrelation causes spurious inferential findings between landscapes and LST, few UHI studies acknowledged spatial autocorrelation or employ appropriate methods (i.e., spatial autoregression) to correct its associated errors during parametric tests.

Improving knowledge on how to optimize urban spatial configuration for remediating UHI remains a prerequisite for creating sustainable cities. Urbanization provides both problems

and solutions for sustainable development (Grimm et al., 2008; Rosenzweig et al., 2010); consequently, the question of what 'optimal' urban form is (Batty, 2008) could reveal much about reaching sustainability. Past research has revealed that land cover composition and configuration, along with other geographical phenomena (i.e., albedo), can explain much of the spatial pattern of UHI yet advances await. In response, this research was made to: (*i*) assess the spatial pattern of mean ambient night temperature across 34 streetscapes in New York City (NYC); (*ii*) create and differentiate global and local regression models between-natural and built landscape characteristics- and mean ambient night temperature; and (*iii*) use geographically weighted regression (GWR) to assess local patterns of correlated associations. Using temperatures recorded at the top of the urban canopy layer (UCL) across 34 NYC weather stations, and landscape metrics calculated from 0.914 m land cover data with 96% accuracy, the central purpose of this paper was to further investigate how urban *streetscape* features combine to impact the UHI. By doing so, this research meant to advance scientific knowledge of the complex urban ecosystem while offering applied insight useful to engineers, architects, urban designers, and sustainable development planners for remediating the negative effects associated with the UHI.

2. Study area

The study area (Fig. 1) for this UHI research incorporated 34 weather stations across four of the five boroughs in New York City (NYC), New York (40°42′46″N, 74°00′21″W). Located on the Eastern Seaboard of the conterminous United States of America, currently with a population of over eight and a half million (U.S. Census, 2017), NYC is classified as an "Alpha ++" World City making it one of the most influential cities in the world. The City has the highest population density of any major city in the United States, with over 11,000 people per square kilometer (NYC, 2017). NYC links its status to the amalgamation of its five: Brooklyn, Manhattan, Queens, Staten Island, and The Bronx. NYC has lengthy shorelines on the Atlantic Ocean, the New York Bay, Long Island Sound, East River, and is positioned at the mouth of the Hudson River. Most of the City's modern footprint occupies the three islands of Manhattan, Staten Island, and Long Island, which are separated primarily by tidal straits. Most of the natural relief has been smoothed through urbanization processes, but elevation changes do exist, with the highest elevation recorded at 125 m above sea level at Todt Hill. The City has an average elevation of roughly 10 m and has a total land area of 789 km^2 (NYSG, 2010). NYC's land use is a heterogeneous mixture of: business districts with towering new and old structures that have increased daytime energy usage; densely populated residential places with increased evening energy usage; less dense residential locations with one and two-family detached dwellings; and many mixed residential and commercial areas, parks and green spaces (Gaffin et al., 2008). Lastly, NYC has gained a green city reputation ("Green Apple"), due to its walkability, far-reaching transit system, and population and built density that makes it an ideal location for studies pertaining to sustainable urbanization (McPhearson, 2011).

Coastal megacities like NYC encounter multifaceted atmospheric circulations including mixing of UHI with continental and regional maritime air masses (Meir et al., 2013). Because of its coastal location in the extreme southeastern portion of New York state, the City is characterized by a marine coastal atmosphere and warm humid subtropical climate (Köppen-Geiger climate type: *Cfa*). According to Köppen-Geiger climate classification, NYC has a temperate climate with warm summers, rainfall throughout the year, and a positive water budget. Four distinct seasons occur in NYC, with the summers considered as warm and humid and winters cold and windy. Over the course of the year, temperatures typically vary from −2°C in January to 29°C in July. Based on climate data recorded at Belvedere Castle in Central Park from 1981 to 2010, NYC has a mean precipitation amount of 1269 mm annually (NRCC, 2018). The precipitation is relatively even throughout the year, often coming in the form of snow in January and February but with limited snow cover. According to Meir et al. (2013), extreme heat events negatively influence thermal comfort and sea breezes positively influence thermal comfort in NYC (Meir et al., 2013). Gedzelman et al. (2003) investigated the climatology for NYC and reported the UHI effect increased in late afternoon, is maximized from midnight to early morning, and non-existent after dawn for a period. In that same study, they found that NYC's UHI had an average magnitude of 4 °C in the summer and autumn and 3 °C in the winter and spring (Gedzelman et al., 2003). Gaffin et al. (2009) and Rosenzweig et al. (2009) went on to depict that the UHI in NYC has temperature differences of roughly 2.5 °C and up to 8 °C when contrasting urban and rural locations, respectively. The power of NYC UHI is so great that it was found to modify both summer daytime thunderstorm formation and movement (Bornstein and LeRoy, 1990; Bornstein and Lin, 2000). Due to recent (i.e., Hurricane Sandy) and projected climate change related natural disasters (see Stocker et al., 2013; Seneviratne et al., 2014; Dutton et al., 2015), its restricted coastal geography, high population density, congested streets, poor air quality, and high urban density and geometry, it is vital that NYC become the most sustainable city in the country (McPhearson, 2011; Hamstead et al., 2016). In sum, by investigating how NYC *streetscapes* related to its UHI, sustainable development planning insight on how to resiliently (re)urbanize at fine scales is provided.

3. Materials and methods

3.1. Urban canopy layer temperatures

There are three types of UHI currently recognized. However, historically the UHI was assessed across two-layers (urban canopy, urban boundary) of urban atmosphere (see Oke, 1976). These two urban atmospheric stratums are commonly referred to as the canopy layer urban heat island (CLUHI) and boundary layer urban heat island (BLUHI). CLUHI is the layer just above the ground and reaches to the average height of buildings, while BLUHI is above the average height of the buildings and extends to the upper limits of urban pollution (Oke, 1976, 2002). The third version of the UHI is the surface urban heat island (SUHI), which is direct surface temperatures most commonly measured through remote sensing methods (Connors et al., 2013). Temperatures for gauging the CLUHI are sampled between 1 and 2 m above the ground (standard screen height) using stationary sites or vehicle traverse, while temperatures for assessing the BLUHI are collected by weather towers, aircraft, or satellites (Voogt and Oke, 2003; Stewart and Oke, 2012). Most recent studies between landscape and UHI have used satellite-based thermal images from Landsat ETM+ (60 m pixels) or ASTER (90 m pixels) platforms (Myint et al., 2013; Song et al., 2014), which are not ideal for assessing micro (~100 m^2) to local (~1 km^2) scale landscapes. Although requests have been made to remotely calculate micro-scale (<10 m) temperatures (Deng and Wu, 2013; Jenerette et al., 2016), those data are not yet freely available for much of the world. Further, LST are recorded at ground-level and are not ideal for capturing the synergistic climate and temperature impacts of three dimensional built and vegetated features within cities (Oke, 1988, 2002; Arnfield, 2003; Voogt, 2007). Although boundary layer temperatures have their place in macroscale studies of UHI,

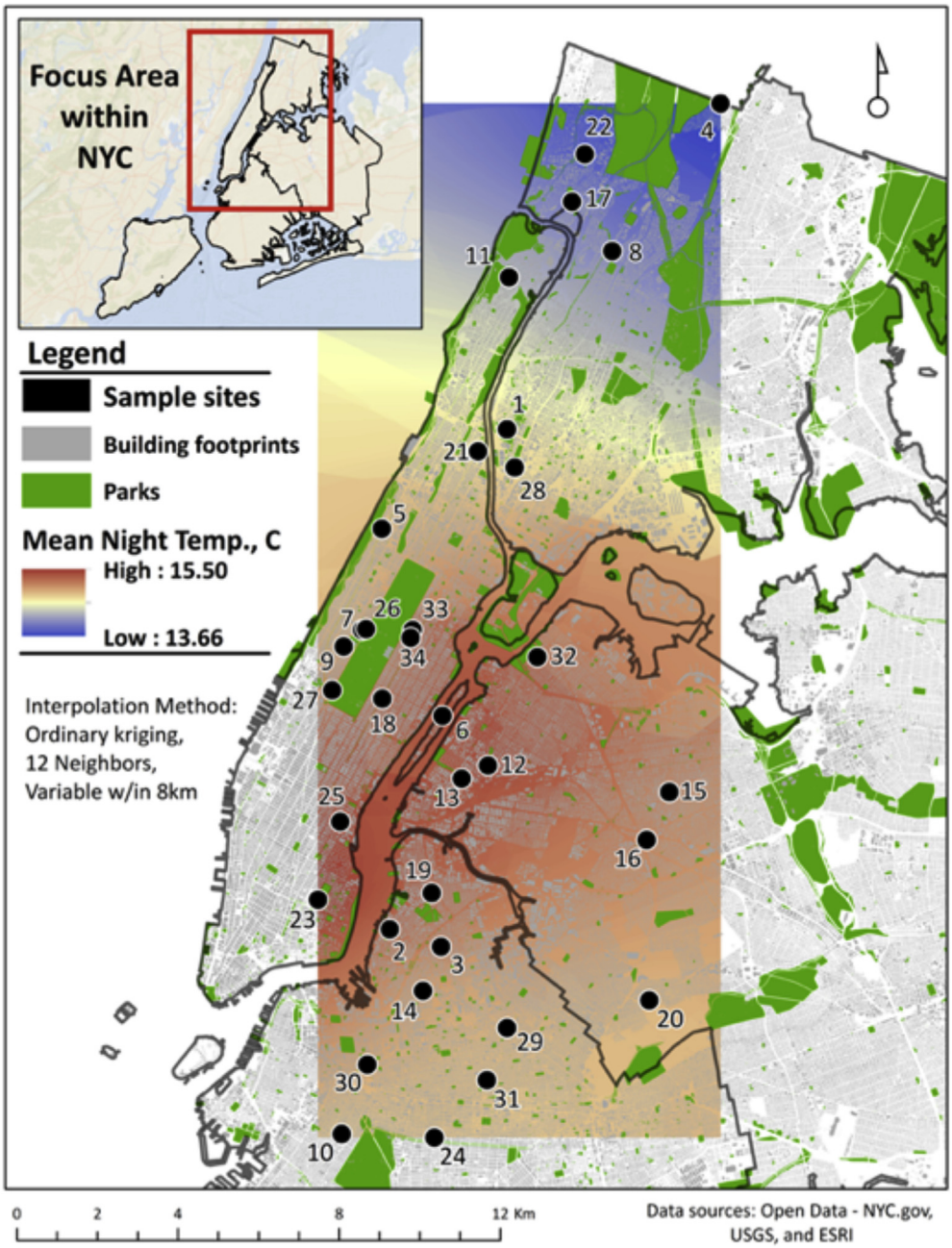

Fig. 1. Study area map of the 34 weather station locations and corresponding streetscapes across New York City. Mean ambient night temperatures, recorded at the urban canopy layer (UCL), were interpolated into a statistical surface using ordinary kriging.

the coarse-grained data from their collection methods were deemed not appropriate for assessing streetscape designs.

Temperatures for this study were recorded at the top of the urban canopy layer (UCL) across 34 intercity weather stations from 24 September 2012 to 25 October 2012. The UCL atmospheric stratum was considered best for evaluating *streetscapes*, which are the extents primarily used during landscape architecture, urban design, and urban resilience planning projects. Also, there are few recent examples of landscape configuration studies using discrete (point-specific) ambient air temperatures in their analyses. Using a geographically stratified sampling technique contingent on available weather stations, UCL temperature data were collected freely from the web applications: Weather Underground (www.wunderground.com/) and WeatherBug (www.weatherbug.com). Most of the weather stations used in this study are owned and operated by: city, state, and federal environmental management agencies; public and private primary and secondary schools; and public and private colleges and universities. In doing so, the temperature measuring equipment was deemed of high scientific quality, appropriate collection methods (i.e., Davis Radiation Shield) used, and data presumed to meet or exceeded standard accuracy = ± 0.5 °C and resolution = 0.1 °C. Temperatures were collected twice a day, at 2pm and 11pm, over the aforementioned one-month time period. Both day and night temperatures were then averaged across the 34 sample sites; 2pm temperatures ranged from 15.71 to 20.12 °C (mean ± SE = 17.11 ± 0.17) and 11pm temperatures ranged from 13.45 to 16.08 °C (mean ± SE = 14.90 ± 0.10). To illustrate the

spatial pattern of the mean night temperatures within this dataset, a raster surface was generated from the 34 site-specific values using the ordinary kriging spatial interpolation technique within ESRI's (2016) ArcGIS 10.4 (Fig. 1). As provided in Appendix Table S1, ordinary kriging allows to statistically validate the prediction surface produced based on its model error statistics. For a kriging spatial interpolation model to provide accurate predictions, the Mean Prediction Error (MPE) should be close to 0, Average Standard Error (ASE) should be as small as possible (below 20), and the Standardized Root-Mean Square Prediction Error (SRMSPE) should be close to 1 (Forsythe et al., 2016, 2018). To further assess the UHI within this dataset, night temperatures for the warmest and coolest weather stations were statistically contrasted and illustrated for the one-month time period (Fig. 2). In doing so, based on a Paired Sample T-Test, a significant difference between night temperatures for the coldest sample location (site #22, Fig. 1; $M = 13.45$, $SD = 3.41$) and the warmest sample location (site #23, Fig. 1; $M = 16.09$, $SD = 3.13$) conditions was recorded; $t(29) = 20.72$, $p < 0.001$. Lastly, since UHI intensity is greatest during nighttime hours (Oke, 1982, 2002), mean nighttime temperature was used as the response (dependent) variable for this study's "hotspot" and subsequent inferential analyses.

3.2. Streetscape characteristics

Urban landscapes investigated in this study, referred to as *streetscapes* herein, were established based on Stewart and Oke (2012) 'local climate zones.' From that work, air corresponding to a local climate zone needs a minimum diameter of 400 m; however, air from adjacent local climate zones may hinder a specific site's temperature if the corresponding landscape is too large (Stewart and Oke, 2012). Therefore, this study's 34 *streetscapes* were created using a radius distance of 250 m from the aforementioned intercity weather stations. Using the 34 *streetscapes* for metric calculation and aggregation, the following eight data categories were used for organizing more than 90 predictor variables: light detection and ranging (LiDAR) derived metrics, urban chasm cross-section, planimetric derived metrics, incoming solar radiation, photosynthesis activity, land cover composition, land cover class configuration, and landscape diversity.

Two *LiDAR derived metrics* were calculated for the 34 streetscapes, which were mean elevation and Northness. LiDAR data for these two predictors came from the bare-earth, hydro-flattened, digital-elevation surface model created for New York City in 2010, and is freely available through the NYC OpenData website (https://opendata.cityofnewyork.us). This Digital Elevation Model (DEM) was generated by interpolating the LiDAR ground points to create a 0.3048 m (1 ft) pixel resolution seamless surface. Cell values correspond to the natural ground elevation value above sea level, with all buildings, trees and other surface features removed (NYC, 2017). Across the 34 streetscapes, descriptive statistics for mean elevation above sea level were: 5.3 ft (min), 63.2 ft (mean), and 162.1 ft (max). In the Northern Hemisphere, south-facing slopes have higher surface temperatures and decrease as the aspect moves from south to north (Sheng et al., 2009). However, since aspect is communicated in circular (360°) data it does not meet the requirement for regression analysis therefore it was converted to the measure Northness using two steps. First, aspect was calculated within ESRI (2016) ArcGIS 10.4, using the Raster Tools and the aforementioned 0.3048 m (1 ft) resolution LiDAR data. Second, following Ivajnšič et al. (2014) lead for deriving Northness to assess a small city's UHI in Slovenia, this solar radiation interception metric was calculated using the following trigonometric function of aspect (*NORTHNESS* = cos (aspect)). In doing so, Northness values are close to negative one (−1) when the aspect is southward, close to zero (0) when the aspect is eastward or westward, and close to positive one (+1) when the aspect is northward.

The *urban chasm cross-section*, or so-called urban canyon, was captured using the Sky-view factor (SVF). SVF was first suggested by Oke (1981) and can be defined as the percentage of sky visible at a location relative to its obstructing buildings, vegetation, and other surface features (Oke, 1988; Upmanis, 1999; Shaker and Drezner, 2010). SVF is a valid metric for capturing built-up proportions that influence UHI (Oke, 1981), because it captures long-wave radiation escape in urban areas (Arnfield, 2003). According to Gal et al. (2007) SVF has become a hallmark proxy of UHI because of its applicability to urban design, urban geospatial data, and spatial analysis techniques. In response, a sizable amount of research supports the theoretical and quantitative link between SVF and UHI (i.e., Eliasson, 1996; Upmanis, 1999; Grimmond et al., 2001; Li et al., 2004; Shaker and Drezner, 2010; Debbage, 2013; An et al., 2014; de Morais et al., 2017; Middel et al., 2018). Several techniques for collecting SVF have been created since its conception; however, all produce an output proportion scaled between 0 and 1 (or 0–100%) and are well-suited for quantifying natural and built streetscape characteristics (Gal et al., 2007). For this study, the method used by Grimmond et al. (2001) to capture SVF using full-sky hemispheric fish-eye lens photography was adopted. Following Shaker and Drezner (2010), but using the upgraded camera Sony a55v DSLR camera in conjunction with a Rokinon attachable fish-eye lens, the complete (all built and natural features) SVF was captured at each streetscape location (Fig. 3). Photos were taken at a height of 10 cm above ground, at street centerline to provide a symmetrical 180-degree view of streetscape features. Each photo contained a total of 3,237,600 pixels, were then converted to black (buildings and coverage) and white (sky) using Adobe Lightroom and summed using the pixel count tool within Photoshop. The SVF, or the ratio of "seeable" sky to streetscape features, was then computed. Lastly, it was conceived SVF would help fleshing-out partial correlations during the forthcoming multiple regression analyses.

Planimetric derived metrics calculated within this study's 34 streetscapes were: mean building height, mean building age, and building density. Source data for these three predictors came from the planimetric database created for New York City, and is freely available through the NYC OpenData website (https://opendata.cityofnewyork.us/). Across the five boroughs, the source imagery for this dataset was circa 2016. All buildings with areas greater than

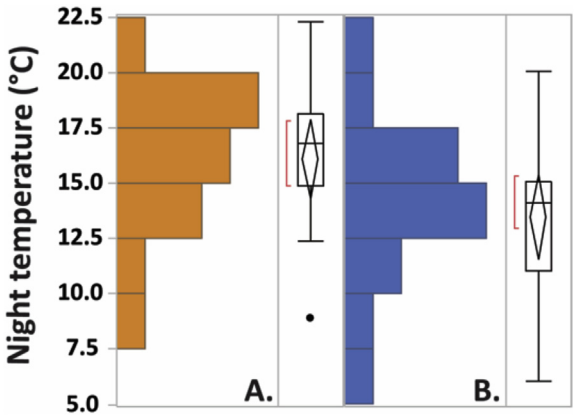

Fig. 2. Night temperature distributions of (A) warmest (site #23, Fig. 1) and (B) coolest (site #22, Fig. 1) weather stations within this study, based on data collected at 11pm from 24 September 2012 to 25 October 2012. Box plot illustrating quartiles (whiskers are ± 1.5 * interquartile range), confidence diamond for mean value, and *shortest half* bracket.

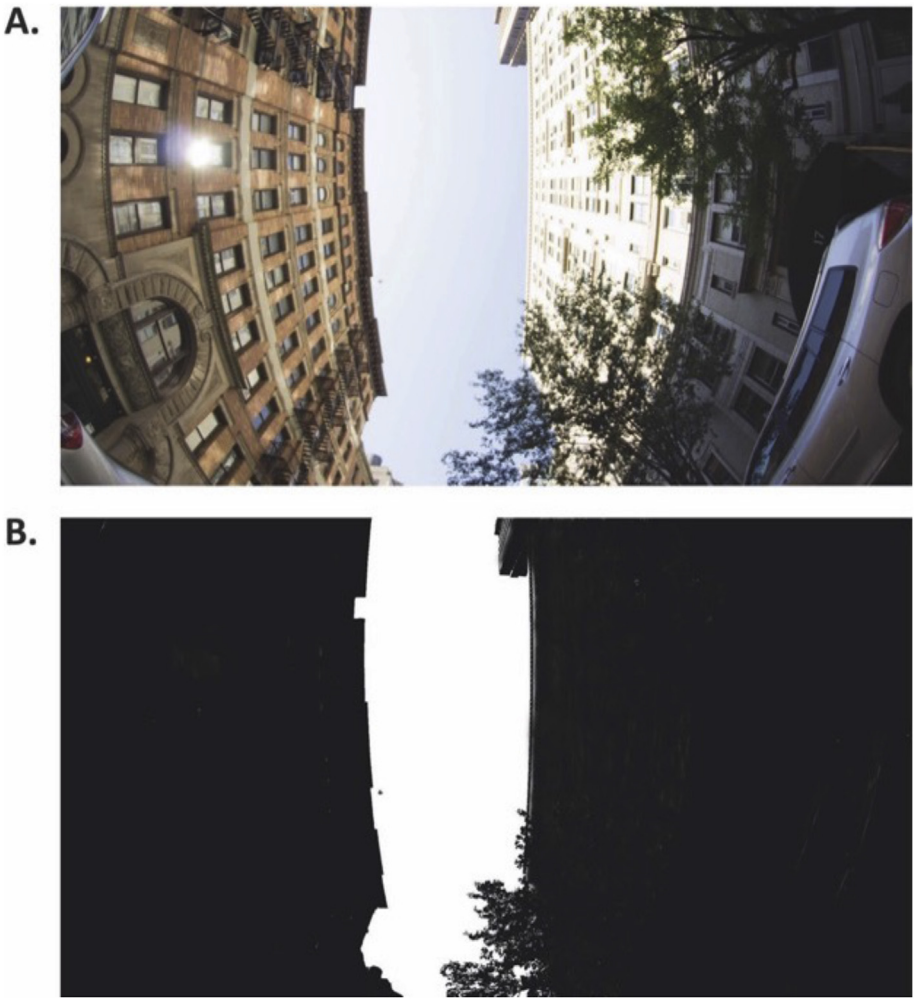

Fig. 3. Percentage visible sky (sky-view factor) as captured through fisheye photography at 89th Street and Madison, in Manhattan (A). After image processing, only 19% of the sky was considered visible at this NYC urban chasm cross-section (B) (sample site #34, Fig. 1).

400 ft^2, without building information numbers (BIN), were collected; albeit all buildings of any size with a BIN were included in the database. Positional correctness for the planimetric data was estimated at 95%, and created using LiDAR and/or photogrammetrically with plus or minus two feet (+/− 2 ft) accuracy (NYC, 2017). Building height was gaged as the difference between building roof elevation and surface elevation (opposed to height above sea level). Across the 34 streetscapes, descriptive statistics for mean building height were: 18.8 ft (min), 53.2 ft (mean), and 158.5 ft (max); mean building age: 1849 (min), 1920 (mean), and 1975 (max); and number of buildings: 15 (min), 319 (mean), and 726 (max). Building density was created by normalizing the number of buildings by streetscape area, which decreased sampling bias and errors related to the modifiable area unit problem (MAUP).

Photosynthesis activity was included by using the mean normalized difference vegetation index (NDVI) for each of the 34 streetscapes. NDVI is calculated from the visible and near-infrared light reflected by vegetation, with healthy vegetation absorbing most of the visible light that hits it and reflecting a larger amount of the near-infrared light (NASA, 2017). Two Landsat 7 Enhanced Thematic Plus (ETM+) images taken on October 5 and October 21, 2012 were downloaded, which falls between Sept. 24, 2012 and Oct. 25, 2012. Since the scan line corrector (SLC) malfunctioned after May 31, 2003, numerous gaps exist on the two Landsat ETM + images. Three steps are processed to derive average NDVI values for the 34 streetscape samples. First, NDVI was computed with the two SLC-off images, respectively. It is computed as a ratio-of the difference of the near infrared band and the red band- and the sum of these two bands. For Landsat 7 images, the NDVI equation can be written as:

$$NDVI = (Band\ 4 - Band\ 3) / (Band\ 4 + Band\ 3)$$

Where Band 4 is near-infrared (0.76–0.90 μm) and Band 3 is red (0.63–0.69 μm). Computations of NDVI for a specific pixel will produce a value that ranges from minus one (−1) to plus one (+1); however, a zero equates to no vegetation (no green leaves) and close to +1 (0.8–0.9) specifies the maximum density of productive green vegetation (NASA, 2017). Second, a simple method was used to fill the gaps. Specifically, the available NDVI pixels from the image taken on October 21, 2012 were assigned to the NDVI map taken on October 5, 2012. Third, after deriving an NDVI map of circa October 2012, the mean NDVI value of all pixels within each of the 34 streetscapes was calculated.

Incoming solar radiation impacts local thermal dynamics (Jahani and Mohammadi, 2018) and was calculated for each of the 34 streetscapes using the Area Solar Radiation tool within Spatial Analyst extension in ESRI (2016) ArcGIS 10.4. This tool calculates

incoming solar radiation into a raster surface for a user specified time-frame. Global radiation pixel values are the total amount of incoming solar insolation for each sample site of the input surface by adding diffuse and direct insolation (ESRI, 2016). A 10-m digital elevation model (DEM), retrieved from the U.S. Geological Survey's National Elevation Database (NED; 2015), was used as the study area's input surface. The spatial resolution was maintained at 10-m and radiation pixel-values were averaged for each of the 34 streetscapes. To correspond with the temperature data collected, the timeframe inputted for was 24 September 2012 to 25 October 2012. The mean latitude of the study area, 40.78°N, was automatically calculated by the Area Solar Radiation tool. The output radiation raster is floating-point type and expressed in watt hours per square meter (WH/m^2).

Land cover composition, *land cover class configuration*, and *landscape diversity* metrics were calculated for each streetscape using the fine spatial and categorical resolution land cover data set created for New York City (NYCPR, 2010; MacFaden et al., 2012). This 2010 land cover raster data has a minimum mapping unit of 3 square feet (0.914 m resolution) and was evaluated to have an overall accuracy of 96%, which both remain originalities within the UHI literature. This high-resolution land cover data set was classified into seven land cover categories: (1) tree canopy, (2) grass/shrub, (3) bare earth, (4) water, (5) buildings, (6) roads, and (7) other paved surfaces. To derive such fine resolution and heightened accuracy, Object-Based Image Analysis (OBIA) was collaboratively employed by the New York City Urban Field Station and University of Vermont's Spatial Analysis Laboratory to create this data set using 2010 LiDAR data, 2008 4-band orthoimagery, and other discrete GIS data including ballfields, building footprints, parking lots, railroads, railroad structures, roads, and surface water. The *land cover composition* (percentages), *configuration*, and *landscape diversity*, metrics were processed using the freeware FRAGSTATS (ver. 4), which computes pattern metrics of land use and land cover (McGarigal et al., 2012). Specifically, compositions were computed for all seven land cover classes; however bare earth, water, and other paved surfaces were omitted from land cover class configuration calculation due to low presence or statistical insignificance of percentages across the 34 streetscapes. The seven land cover categories for the 34 streetscapes yielded the following compositions: buildings (33.8%), other paved surfaces (23.3%), tree canopy (20.3%), roads (16.0%), grass/shrub (6.5%), bare earth (0.1%), and water (0.1%) (percentages from this study). Since no winning set of landscape ecology metrics has been recognized for assessing landscape structure (Riitters et al., 1995; Wagner and Fortin, 2005), 25 area-weighted class configuration metrics were processed for each of the four land cover classes tree canopy, grass/shrub, buildings, and roads. Lastly, two landscape diversity measures, Shannon's diversity index (SHDI) and Shannon's evenness index (SHEI), were computed for each of the 34 streetscapes.

3.3. Data analysis

To fulfill the three objectives of this paper, a five-step spatial analysis was fashioned to evaluate the geographical pattern of NYC's UHI across the study area, and to statistically test its relationship to natural and built streetscape characteristics. To meet the Gaussian distribution prerequisite for parametric tests, variables were transformed using common techniques (i.e., log, logit, arcsine) to improve their normality where relevant. The Shapiro-Wilk normality test was computed in the statistical software JMP (ver. 13; SAS, 2016) to establish if transformation was needed, and which mathematical operation aided in reaching Gaussian frequency. Justification and specific details of the five-step method are outlined in the following paragraphs of this section.

(1) First, exploratory spatial data analysis (ESDA) was used to evaluate the level of spatial autocorrelation of mean ambient night temperature and the over 90 streetscape predictors of this study. 'Spatially close things are more similar than remote things' is a phenomenon known as the First Law of Geography (Tobler, 1970). This geographical fact is translated as a variable's level of spatial autocorrelation, which is further deduced as a variable's univariate level of numerical dependence (cross-correlation, non-randomness, non-stationarity) based on its geographical position in reference to a predetermined number of its neighboring values. Spatial autocorrelation is commonplace to socio-economic and environmental data, and can be an advantage and disadvantage when investigating spatial patterns of inference. A benefit of spatial non-randomness is that indicator patterns can be statistically evaluated and contrasted to urban resilience and sustainability (Shaker, 2015). However, the existence of spatial autocorrelation defies the requirement of randomness thus global parametric statistics (i.e., ordinary least squares; OLS regression) may not be suitable for investigating inferential associations (Lichstein et al., 2002; Dormann et al., 2007). With geospatial technology and new spatial analysis progressing, by the end of 20th century it was argued that all previous spatially-related research now take spatial autocorrelation into account (Lennon, 2000). In this study, both global and local versions of ESDA were used to evaluate spatial non-stationarity using ESRI (2016) ArcGIS 10.4 Spatial Analyst Tools. Specifically, Global Moran's *I*-test (Moran, 1950) was used to appraise geographical non-stationarity of all variables, and Getis-Ord Gi* (Getis and Ord, 1992) was used to conduct a "hot spot" analysis of mean ambient night temperature. For both Global Moran's *I* and Getis-Ord Gi* tests, the distance parameter of 8 km was chosen for the Incremental Spatial Autocorrelation tool within ArcGIS, with conceptualization of spatial relationships Euclidean inverse distance weighting (IDW). The Global Moran's *I* equation can be described as:

$$I = \frac{n}{s_o} \frac{\sum_{i=1}^{n}\sum_{j=1}^{n} w_{i,j} z_i z_j}{\sum_{i=1}^{n} z_i^2}$$

where z_i is the deviation of an attribute for item *I* from its mean ($z_i - \overline{X}$); $w_{i,j}$ is the spatial weight between item *i* and *j*; *n* is equal to the total number of items; and s_0 is the aggregate of all the spatial weights. Note that Getis-Ord Gi* is a local index of spatial association (LISA) because it illustrates where the significant spatial clusters are located by returning a z-score for each attribute being evaluated. For statistically significant negative z-scores, the smaller the z-score, the stronger the clustering of low values (cold spot); for positive z-scores, the larger the z-score, the stronger the clustering of high values (hot spot; ESRI, 2016). The Getis-Ord Gi* test can be described as:

$$G_i^* = \frac{\sum_{j=1}^{n} w_{i,j} x_j - \overline{X} \sum_{j=1}^{n} w_{i,j}}{s \sqrt{\frac{\left[n \sum_{j=1}^{n} w_{i,j}^2 - \left(\sum_{j=1}^{n} w_{i,j}\right)^2\right]}{n-1}}}$$

where x_j is the attribute value for item *j*; $w_{i,j}$ is the spatial weight between item *i* and *j*; *n* is equal to the total number of items; and:

$$\overline{X} = \frac{\sum_{j=1}^{n} x_j}{n}$$

$$s = \sqrt{\frac{\sum_{j=1}^{n} x_j^2}{n} - (\overline{X})^2}$$

The G_i^* statistic is a z-score so no additional computations are necessary (ESRI, 2016). Lastly, to help illustrate the spatial patterns of NYC's UHI, an interpolated surface was created from the Getis-Ord Gi* z-scores using the IDW method (Fig. 4).

(2) Second, bivariate relationships between-natural and built streetscape characteristics- and mean ambient night temperature were explored using two techniques. Initially, a two-tailed Pearson's Product-Moment Correlation test (r) was used to evaluate associations between mean ambient night temperature and the 90 + explanatory streetscape particularities. Successively, bivariate ordinary least squares (OLS) regression was utilized to create scatterplots, visualize slopes, and attain predicted expressions of key statistically significant relationships. Pearson's correlation coefficients and OLS's coefficient of determination (R^2) both range from 1 to −1, with values closer to 1 indicating stronger predictive associations. They are two of the most common global inferential tests for understanding bivariate interactions, and a P-value complements the coefficient score indicating its statistical significance. Thirty-six natural and built

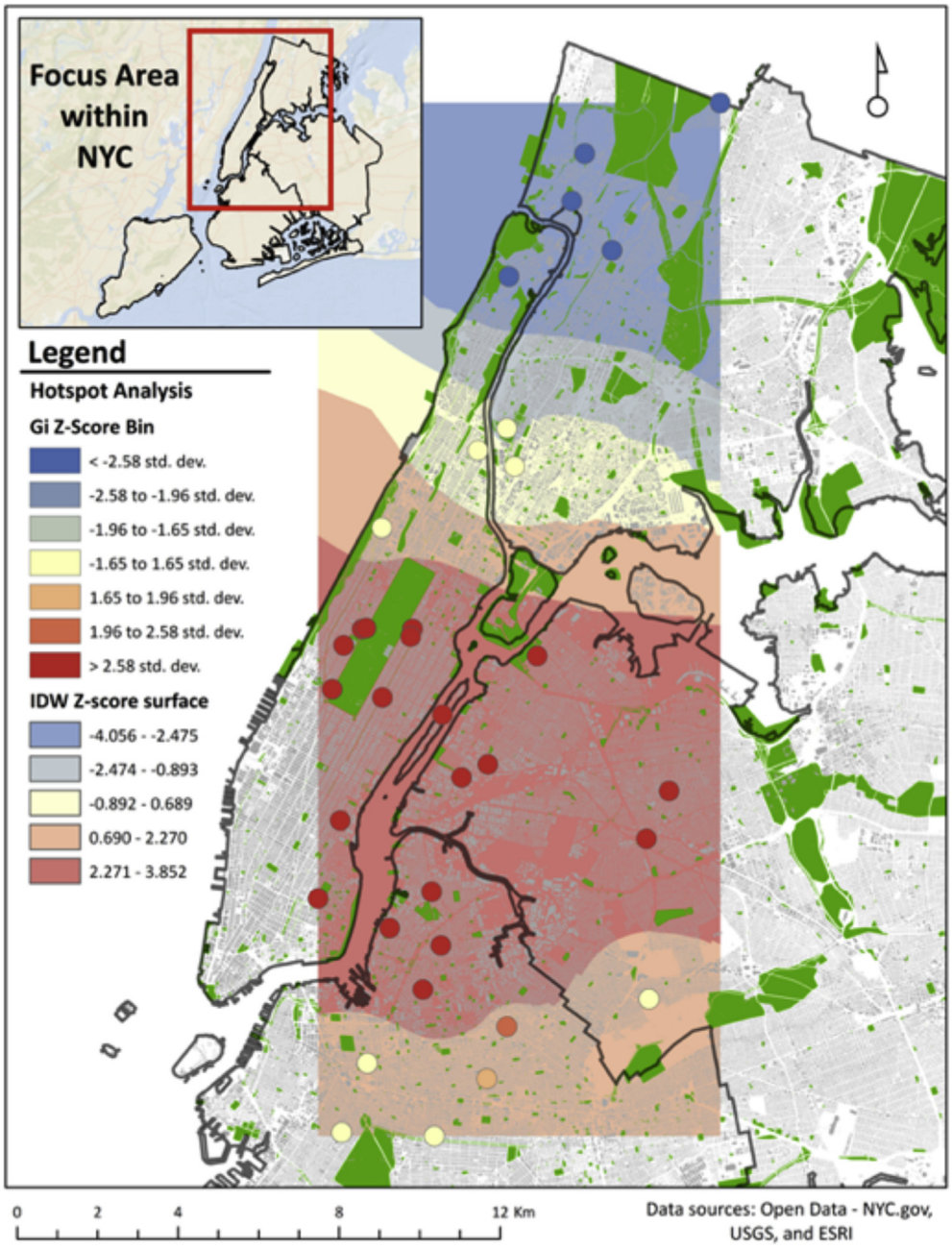

Fig. 4. Local index of spatial associations (LISA) illustration of mean ambient night temperature across the 34 study area streetscapes using the Getis-Ord Gi* statistic. The neighborhood distance parameter was investigated and set to 8 km; cold and hot spots were illustrated using z-scores at sample sites and interpolated z-scores using inverse distance weighting (IDW).

characteristics (Data S1) had at least marginally significant Pearson's correlations with mean ambient night temperature across the 34 streetscapes ($P < 0.10$, Table 1). Lastly, to eliminate unsound bivariate regressions, the Shapiro-Wilk test was employed to assess the normality of residuals. Twelve OLS bivariate regressions between-natural and built streetscape characteristics- and mean ambient night temperature were visualized into scatterplots ($P < 0.05$, Figs. 5 and 6). The statistical program JMP (ver. 13; SAS, 2016) was utilized here.

(3) Third, to achieve the second and third objectives of this research, this study assessed synergies of natural and built streetscape characteristics through multiple regression analysis. From the previous Pearson's correlation test, 28 of the 36 streetscape predictors were included in the exploratory multiple regression analysis. Eight variables were removed because they were highly skewed and/or lacked variability. By means of multi-model selection framework (Burnham and Anderson, 2003; Diniz-Filho et al., 2008), within the freeware Spatial Analysis in Macroecology (SAM)

Table 1
Global spatial autocorrelations for all study variables using Global Moran's *I*-test; Pearson product-moment correlation coefficients (two-tailed) between average ambient night time temperature and all significant ($P < 0.10$) landscape form predictors across New York City streetscapes ($n = 34$).

	Global Moran's *I*	z-score	*P*-value	Pearson's *r*	*P*-value
Dependent variable					
Mean ambient night temperature	0.289	2.675***	0.007		
LiDAR derived metric †					
Mean elevation	0.236	2.187**	0.029	**−0.523**	**0.002**
Urban chasm cross section ‡					
Sky-view factor	0.258	2.385**	0.017	**−0.719**	**<0.001**
Land cover composition ‡					
Tree canopy, percent	0.325	3.072***	0.002	**−0.389**	**0.023**
Grass/shrub, percent	0.044	0.631	0.528	−0.331	0.056
Buildings, percent	0.054	0.699	0.484	**0.373**	**0.030**
Roads, percent	0.115	1.245	0.213	0.337	0.052
Tree canopy class configuration ‡					
Total class area (CA)	0.334	3.052***	0.002	−0.328	0.058
Largest patch index (LPI)	0.470	4.398***	<0.001	**−0.397**	**0.020**
Area-weighted patch area distribution (AREA_AM)	0.468	4.426***	<0.001	**−0.404**	**0.018**
Area-weighted mean of shape index (SHAPE_AM)	0.374	3.507***	<0.001	**−0.397**	**0.020**
Area-weighted mean of fractal area dimension (FRAC_AM)	0.334	3.080***	0.002	**−0.347**	**0.044**
Area-weighted mean of core area distribution (CORE_AM)	0.459	4.360***	<0.001	**−0.412**	**0.015**
Area-weighted mean of core area index (CAI_AM)	0.472	4.144***	<0.001	**−0.354**	**0.040**
Area-weighted mean of proximity index distribution (PROX_AM)	0.242	2.242**	0.025	−0.334	0.053
clumpiness index (CLUMPY)	0.326	2.933***	0.003	−0.307	0.077
Percentage of like adjacencies (PLADJ)	0.340	3.082***	0.002	**−0.371**	**0.031**
Connectance index (CONNECT)	0.003	0.293	0.769	−0.333	0.054
Patch cohesion index (COHESION)	0.340	3.074***	0.002	−0.326	0.060
Landscape division index (DIVISION)	0.075	1.366	0.172	**0.450**	**0.008**
Effective mesh size (MESH)	0.278	3.057***	0.002	**−0.45**	**0.008**
Aggregation index (AI)	0.343	3.098***	0.002	**−0.375**	**0.029**
Grass/shrub class configuration ‡					
Total class area (CA)	0.093	1.073	0.283	−0.294	0.091
Patch density (PD)	0.074	0.890	0.373	−0.321	0.064
Area-weighted mean of fractal area dimension (FRAC_AM)	−0.001	0.240	0.810	0.323	0.062
Percentage of like adjacencies (PLADJ)	0.152	1.510	0.131	−0.314	0.070
Aggregation index (AI)	0.154	1.527	0.127	−0.311	0.074
Buildings class configuration ‡					
Total class area (CA)	0.042	0.598	0.550	**0.403**	**0.018**
Percentage of like adjacencies (PLADJ)	0.032	0.531	0.596	0.288	0.099
Patch cohesion index (COHESION)	0.279	2.721***	0.007	**0.347**	**0.045**
Roads class configuration ‡					
Total class area (CA)	0.055	0.724	0.469	**0.366**	**0.033**
Largest patch index (LPI)	0.102	1.107	0.268	0.316	0.069
Landscape shape index (LSI)	0.092	1.054	0.292	0.302	0.082
Area-weighted mean of shape index (SHAPE_AM)	0.084	0.935	0.350	**0.437**	**0.010**
Area-weighted mean of fractal area dimension (FRAC_AM)	0.064	0.771	0.441	**0.488**	**0.003**
Patch cohesion index (COHESION)	0.064	0.785	0.432	**0.456**	**0.007**
Photosynthesis activity ‡					
Mean normalized difference vegetation index (NDVI)	0.300	2.802***	0.005	**−0.551**	**0.001**

Symbol designations: † Light Detection and Ranging (LiDAR) data has 0.3048 m (1 ft) pixel resolution; ‡ associated variables calculated for a 250-m radius streetscape from its corresponding temperature sample site.
Technical notes: Landscape ecology metrics computed based on land cover data with 0.9144 m (3 ft) pixel resolution, and using queen contiguity (8-neighborrule); search area for isolation/proximity metrics was 20 m; edge depth for core area calculations was 5 m.Spatial autocorrelation was determined using a threshold distance of 8 km; associated symbols: *** < 1%, ** < 5%, * < 10% chance random pattern.A Pearson's correlation coefficient in bold depicts a statistically significant relationship greater than the 95% confidence level.See Leitão et al. (2012) and McGarigal et al. (2012) for landscape ecology metric details and equations.

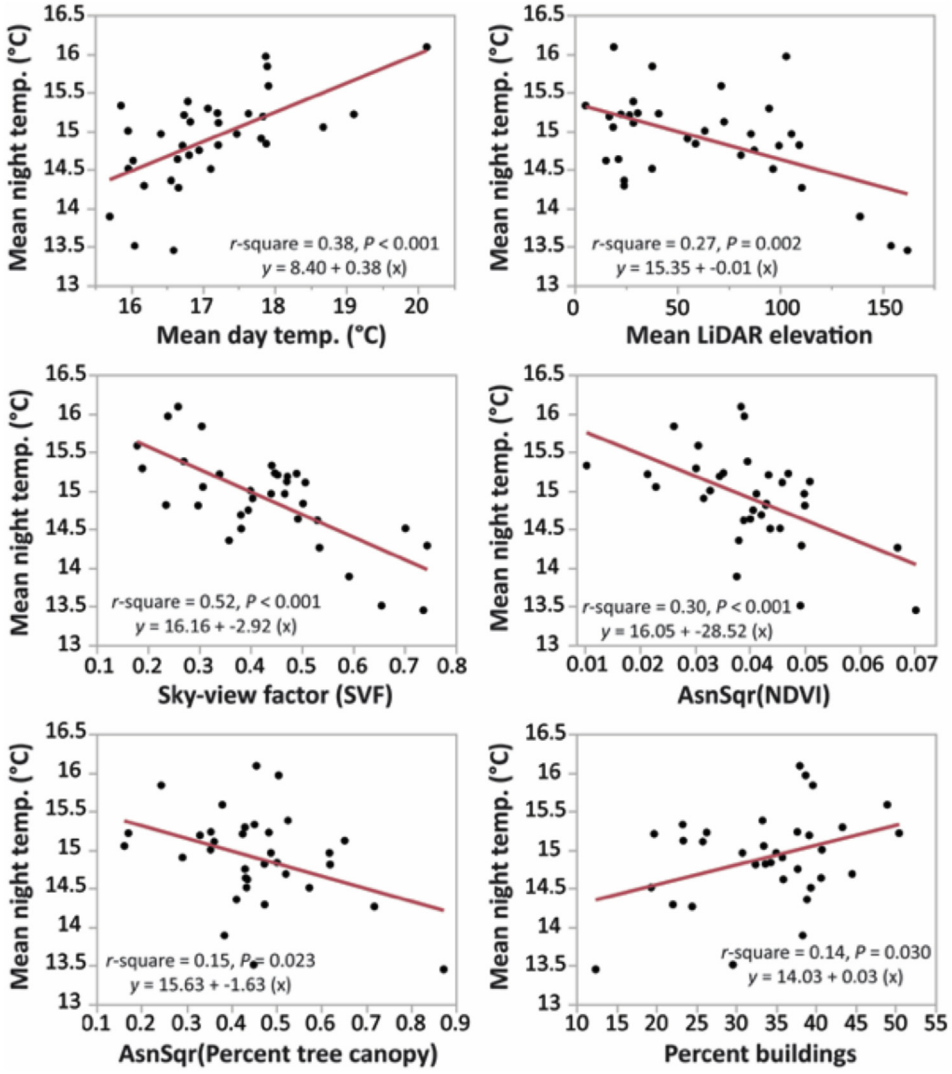

Fig. 5. Significant bivariate relationships between-mean ambient night temperature- and mean ambient day temperature, elevation, sky-view factor (SVF), mean normalized difference vegetation index (NDVI), and land cover class composition metrics ($P < 0.05$; $n = 34$).

(ver. 4; Rangel et al., 2010), the 28 natural and built streetscape characteristics were combined to test all possible global multiple regression models (i.e., 268,435,455) for predicting mean ambient night temperature. The multimodel selection framework computes the Akaike weight (w_i) of each model; w_i is an Akaike information criterion (AIC)-derived metric that grades the likelihood model $_i$ is the best predictive model amid all conceivable models created (Burnham and Anderson, 2003). The six prominent models were picked because of their overall fitness using coefficient of determination (R^2) and corrected (AICc). According to Fotheringham et al. (2004), AICc (Akaike, 1978) is an improved metric of model fitness and estimate of reality. He also noted that a 'serious' distinction between two models is when AICc values diverge by at least three (Fotheringham et al., 2004). Directionality of covariates, and to evaluate their relative impact (rank effects) on mean night temperature, standardized coefficients (beta weights; β) were used to gauge the streetscape predictors across the six multiple regressions. To assess multicollinearity the variance inflation factor (*VIF*) was recorded for each model. *VIF* > 10 explicitly denotes multicollinearity violations; *VIF* > 2.5 denotes conceivable multicollinearity issues. Lastly, the Shapiro-Wilk normality examination was applied to assure independence of model residual and thus randomly distributed errors. The six global multiple regression models (Table 2) were reassessed in the proceeding step using local multiple regression.

(4) Fourth, to fully achieve the second and third objectives of this research, geographically weighted regression (GWR; Fotheringham et al., 2003) was employed to assess local patterns of correlated associations. Conventional global regression (i.e., OLS) should only be utilized when attribute independence and spatial randomness is guaranteed (Shaker et al., 2017). These requirements are often hard to meet, especially with weather and climate data where many processes are non-stationary (Szymanowski and Kryza, 2012). Therefore, a local inferential statistical method such as GWR is more appropriate when spatially non-random variables are under investigation. GWR, a refinement to global regression, includes neighboring effects through a distance decay-weighted philosophy that explicitly deals with the spatial non-stationarity of inferential relationships

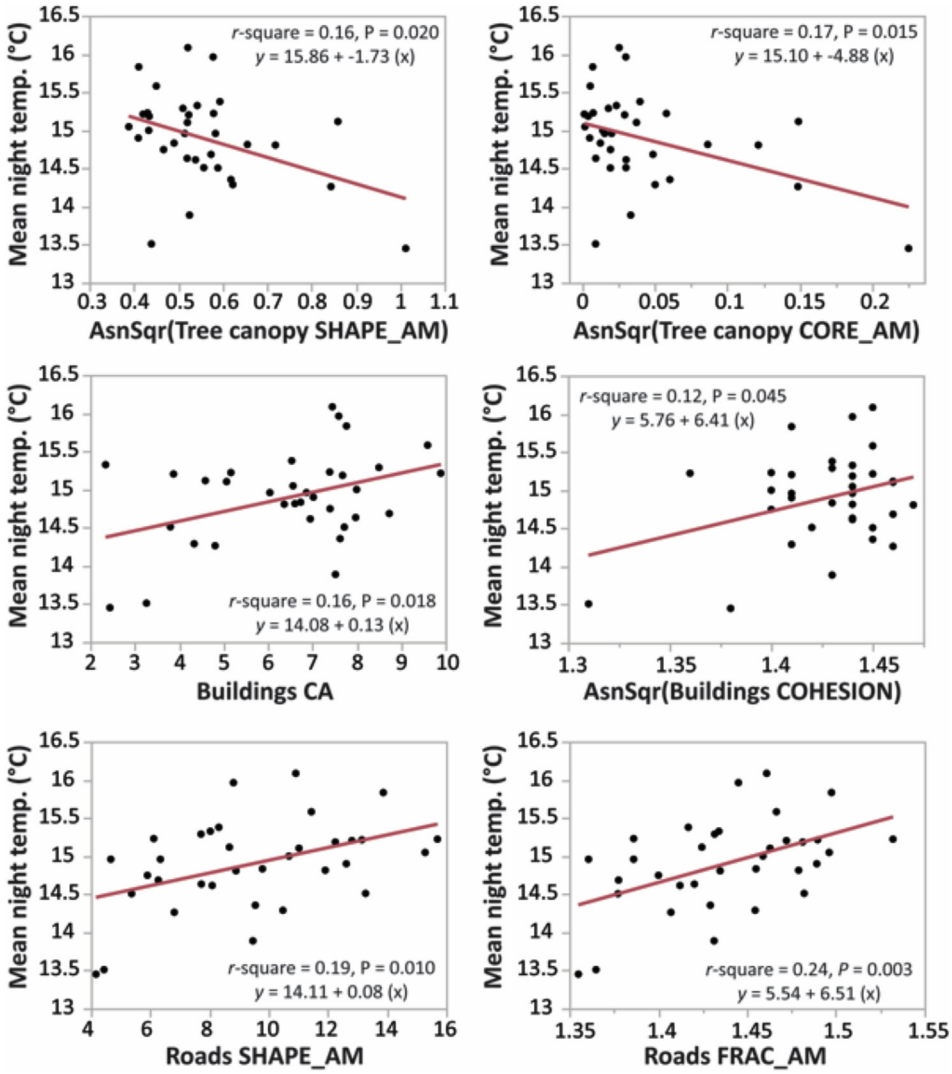

Fig. 6. Significant bivariate relationships between-mean ambient night temperature- and land cover class configuration metrics ($P < 0.05$; $n = 34$).

(Fotheringham et al., 2004). Specifically, GWR is a non-parametric modeling method that applies a series of locally linear regressions to generate estimates for every sample across the study area through a spatial drift of neighboring observations (Fotheringham et al., 2003; Wheeler, 2014). The number of neighbors, or spatial weighting, is captured via spatial kernel function depending on data type and freely available software now allows for Logistic, Poison, or Gaussian (Nakaya et al., 2014). Since GWR operates using neighboring observations it is not suitable for extrapolation beyond its study area that it was established (Shaker and Ehlinger, 2014); however, GWR models are considered more suitable for local descriptive and predictive reasons (Foody, 2003). Since GWR uses a spatial drift method of selecting nearby information through a moving window, it can reduce or eliminate errors produced by spatial autocorrelation when inferential modeling (Kupfer and Farris, 2007).

Regarding previous inferential analyses of UHI, most studies have employed global statistical methods, which do not account for spatial autocorrelation and fail at deciphering local inferential patterns appropriately. Thus, GWR was utilized to remediate errors caused by spatial non-stationarity, and map local patterns of statistically significant streetscape predictors. Within the SAM software (ver. 4; Rangel et al., 2010), the six previously created global multiple regressions were reassessed by GWR modeling module. To aid in understanding the importance of the covariates across the GWR models, all streetscape predictors used in the OLS multiple regression models were standardized using a z-transformation to set all variables to a mean of 0 and variance of 1. Specifically, GWR was employed using an adaptive Gaussian kernel and the Golden Section Search, which selects the optimal number of neighbors (spatial weighting; kernel bandwidth) for minimizing the model's AICc. A typical GWR model is described as (Fotheringham et al., 2003):

$$y_i = \beta_0(u_i, v_i) + \sum_k \beta_k(u_i, v_i) x_{ik} + \varepsilon_i$$

where (u_i, v_i) signifies the coordinates of the response variable y; where (u_i, v_i) signifies the coordinates of i; β_0 and β_k embody the local estimate intercept and influence of predictor k at location i, respectively; and ε is the random error term to account for changing values across space. That said, the key to the GWR equation is locations closer to i have a stronger effect on the calculation of $\beta_k(u_i, v_i)$ than locations further away (Rybarczyk,

2018). The most commonly used Gaussian distance-decay kernel function is described as:

$$w_{ij} = exp\left[-\frac{d_{ij}}{\theta^2}\right]$$

where d_{ij} is the distance between observation i and j and θ is the bandwidth. To assure model fitness, Global Moran's I test (Moran, 1950) was used to appraise spatial autocorrelation for each of the GWR model's residuals. Akin to the OLS multiple regression, the six GWR models were contrasted based on their overall fitness using corrected (AICc) and coefficient of determination (R^2). Once non-stationarity was tested for, and model fitness set, local regression statistics and parameter estimates were illustrated for the most informative predictive model.

(5) Fifth, a two-tailed Pearson's Product-Moment Correlation (r) matrix was employed as an *ex post facto* collinearity evaluation of key statistically significant streetscape predictors of mean night temperature. Pearson's correlation is often used as a data reduction technique to decrease the likelihood of multicollinearity prior to creating multiple regression (Dormann et al., 2013). However, in doing so, important knowledge regarding relationships between natural and built streetscape characteristics would not be disseminated. To help elucidate scientific understanding of the complex urban ecosystem, and reduce the negative effects associated with the UHI, scientific knowledge dissemination is paramount for the sustainable development process. For interpretation purposes, correlation coefficients were organized into very positive (>0.75), positive (0.75–0.50), neutral (0.50 to −0.50), negative (−0.50 to −0.75), or very negative (<−0.75). The JMP software (ver. 13; SAS, 2016) was used again here.

4. Results

4.1. Exploratory spatial data analysis

Taking the spatial relationships of the 34 streetscapes into account, Global Moran's I-test revealed varying levels of spatial non-stationarity for the dependent variable and 36 statistically significant streetscape predictors (Table 1). 15 of the aforementioned natural and built characteristics, and the response variable, had less than 1% chance of occurring randomly using the previously established 8 km distance threshold. Specifically, the response variable's (mean ambient night temperature) spatial frequency recorded a Moran's I score and z-score of 0.29 and 2.68, respectively. Three streetscape predictors also rendered spatial patterns with less than a 5% chance of occurring randomly.

When examining the local distribution of mean ambient night temperature across the 34 sample streetscapes of New York City, the Getis-Ord Gi* statistic illustrated one statistically significant "hot spot" and statistically significant one "cold spot" (Fig. 4). The large and contiguous hot spot takes place over the south-central part of the study area. The most significant hot spot area, at the 1% level, ranged from the northern horn of Brooklyn (Crown Heights to Greenpoint) in the south to the East River border of Queens in the north (College Point, East Elmhurst and LaGuardia Airport). Spanning perpendicular to west, the hot spot stretched to the Hudson River in the Upper West Side neighborhood of Manhattan, south through Midtown and the East Village. The significant cold spot area, at the 1% level, was found in the northwest area of the Bronx. Specifically, the cold spot ranging from Bronx Zoo in the southeast, across to Inwood Hill Park in the southwest, and northward to North Riverdale and Van Cortlandt Park. Although the west and east margins of NYC's UHI cannot be delineated through this hot spot analysis, it does illustrate the central area of concern for this anthropogenic climate alteration.

4.2. Bivariate analyses

Of the over 90 natural and built streetscape characteristics investigated as explanatory variables of mean ambient night temperature, 21 of 36 streetscape predictors had statistically significant relationships greater than the 95% confidence level (Table 1). Using the eight data categories for organizing streetscape predictors from the methods section, 16 of the 21 statistically significant bivariate relationships came from land cover class configuration variables. From the remaining five significant bivariate relationships, two were grouped into the land cover composition category, while LiDAR derived metrics, urban chasm cross-section, and photosynthesis activity all had one variable. The three data categories-planimetric derived metrics, photosynthesis activity, and landscape diversity-did not render bivariate statistical significance using Pearson's correlation test. Within the land cover class configuration data category, ten of the 16 statistically significant bivariate relationships were tree canopy class configuration metrics, four were road class configuration metrics, and two were building class configuration metrics. Since 25 configuration metrics were originally calculated for each of the four land cover class, these preliminary findings are suggestive of tree canopy configuration being more important to UHI than composition and configuration of the other land cover types. That said, overall the two strongest positive predictors of mean ambient night temperature were area-weighted mean of fractal area dimension (FRAC_AM) for roads ($r = 0.49$, $P = 0.003$) and patch cohesion index (COHESION) for roads ($r = 0.46$, $P = 0.007$). Overall, the two strongest negative predictors of mean ambient night temperature were sky-view factor (SVF; $r = -0.72$, $P < 0.001$) and mean normalized difference vegetation index (NDVI; $r = -0.55$, $P = 0.001$). Other notable positive explainers of mean ambient night temperature were: landscape division index (DIVISION) for tree canopy ($r = 0.45$, $P = 0.008$); area-weighted mean shape index (SHAPE_AM) for roads ($r = 0.44$, $P = 0.010$); total class area (CA) for buildings ($r = 0.40$, $P = 0.018$); percent buildings ($r = 0.37$, $P = 0.030$); and patch cohesion index (COHESION) for buildings ($r = 0.35$, $P = 0.045$). Other notable negative explainers of mean ambient night temperature were: mean elevation ($r = -0.52$, $P = 0.002$); effective mesh size (MESH) for tree canopy ($r = -0.45$, $P = 0.008$); area-weighted mean of core area distribution (CORE_AM) for tree canopy ($r = -0.41$, $P = 0.015$); area-weighted mean of shape index (SHAPE_AM) for tree canopy ($r = -0.40$, $P = 0.020$); and percent tree canopy ($r = -0.39$, $P = 0.023$).

The OLS bivariate analysis resulted in twelve statistically sound regression scatterplots ($P < 0.05$, Figs. 5 and 6), which help to explain relationships between streetscape characteristics and mean night temperature. Overall, mean ambient night temperature was best explained by SVF ($R^2 = 0.52$, $P < 0.001$), and was negatively associated ($\beta = -0.72$). The next two strongest negative predictors were mean NDVI ($R^2 = 0.30$, $P < 0.001$) and mean elevation ($R^2 = 0.27$, $P = 0.002$). Regarding land cover class configuration metrics, FRAC_AM for roads was the best predictor of mean night temperature ($R^2 = 0.24$, $P = 0.003$), and was positively associated ($\beta = 0.49$). SHAPE_AM for roads also had a reasonable prediction of ambient night temperature ($R^2 = 0.19$, $P = 0.010$), and was positively associated ($\beta = 0.44$). Note that this study revealed an expected positive ($\beta = 0.62$) and highly significant relationship between mean day and night temperatures ($R^2 = 0.38$, $P < 0.001$).

Table 2
Ordinary least squares (OLS) regression modeling results, standardized coefficients, and individual *p*-values of independent variables significantly related to average ambient night time temperature across 34 New York City streetscapes.
[Covariate values are OLS regression standardized coefficients; values enclosed in parentheses are individual *p*-values. Independent model variables have been transformed to meet normality.].

Statistical measures and independent variables	Models					
Statistical measures	Model 1	Model 2	Model 3	Model 4	Model 5	Model 6
Akaike's Information Criterion (AICc)	27.677	28.935	43.013	43.804	45.605	46.522
R-Square	0.732	0.698	0.614	0.605	0.583	0.572
F	27.263	35.815	11.527	11.096	10.149	9.686
Model *P*-value	<0.0001	<0.0001	<0.0001	<0.0001	<0.0001	<0.0001
Variance Inflation Factor (VIF) max value	1.054	1.020	1.434	1.449	1.458	1.272
Independent variables						
OLS regression standardized constant	0.000 (<0.001)	0.000 (<0.001)	0.000 (<0.001)	0.000 (<0.001)	0.000 (<0.001)	0.000 (<0.001)
LiDAR derived metric †						
Mean elevation	−0.433 (<0.001)	−0.430 (<0.001)	−0.346 (<0.001)	−0.398 (0.005)	−0.408 (0.006)	−0.508 (<0.001)
Urban chasm cross section ‡						
Sky-view factor	−0.624 (<0.001)	−0.658 (<0.001)	–	–	–	–
Planimetric derived metric ‡						
Mean building height	–	–	0.406 (<0.001)	0.550 (<0.001)	0.520 (<0.001)	0.398 (0.006)
Tree canopy class configuration ‡						
Area-weighted mean of shape index (SHAPE_AM)	–	–	–	−0.335 (0.024)	–	–
Largest patch index (LPI)	–	–	–	–	−0.285 (0.059)	–
Buildings class configuration ‡						
Total class area (CA)	–	–	–	–	–	0.221 (0.094)
Roads class configuration ‡						
Landscape shape index (LSI)	0.187 (0.062)	–	0.477 (<0.001)	0.449 (0.002)	0.448 (0.002)	0.411 (0.006)
Photosynthesis activity ‡	–					
Mean normalized difference vegetation index (NDVI)	–	–	−0.352 (0.017)	–	–	–

Symbol designations: † Light Detection and Ranging (LiDAR) data has 0.3048 m (1 ft) pixel resolution; ‡ associated variables calculated for a 250-m radius streetscape from its corresponding temperature sample site, and dash, –, indicate no statistically significant relationship observed.
Technical notes: Landscape ecology metrics computed based on land cover data with 0.9144 m (3 ft) pixel resolution (NYC, 2015), and using queen contiguity (8-neighbor rule); search area for isolation/proximity metrics was 20 m; edge depth for core area calculations was 5 m.

The two global bivariate techniques used in this study, Pearson's correlation test and OLS regression, corroborated that NYC's UHI is affected by both natural and built streetscape characteristics. Additionally, these global bivariate results affirmed that landscape configuration metrics are stronger predictors of UHI than composition measures.

4.3. Global and local multiple regressions

The multi-model selection framework resulted in six OLS multiple regression models for explaining mean ambient night temperature across the 34 NYC streetscapes (Table 2). This method for selecting multiple regressions disregarded 20 of the 28 natural and built streetscape characteristics. Eight predictors were employed across the six distinct global regression models to explain between 57 and 73% of the variation of mean night temperature as expressed by their R^2 values. Models were ranked and numbered based on their AICc values, with Model 1 best-fitting (AICc = 27.68) increasing to Model 6 as worst-fitting (AICc = 46.52). Maximum *VIF* values ranged between 1.02 and 1.46 across the six models, therefore multicollinearity errors linked to covariates were deemed absent. Model 2 included two independent variables; Model 1 used three independent predictors; while the other four models incorporated four independent parameters. The Shapiro-Wilk test divulged normality of residuals and thus randomly dispersed errors across all six global multiple regressions.

The six distinct OLS models allowed for understanding separate and synergistic influences of natural and built streetscape characteristics on mean ambient night temperature. Across the six global multiple regressions, mean elevation was the only constant predictor of mean ambient night temperature. This covariate had an anticipated negative relationship with temperature and was significant well above the 99% confidence level for each model. Landscape shape index (LSI) for roads was the second most present parameter for predicting mean ambient night temperature, with consistent positive directionality and representation in five of the six models. In tandem with other predictors, this important covariate was significantly above the 99% confidence level across four models and marginally significant at the 90% confidence level for one model. Mean building height was the third most present parameter for predicting mean ambient night temperature, with consistent positive directionality and representation in four of the six models. When combined with other independent variables this covariate was well above the 99% confidence level across the four models. Mean building height was considered the second strongest predictor of mean night temperature across all models as signified by its standardized beta coefficients. Sky-view factor was the fourth most present parameter with representation in two of the six models and was negatively directed in both models. Overall, sky-view factor was considered the strongest predictor of mean night temperature across all models as expressed by its standardized beta coefficients. The following three parameters were negatively associated with mean ambient night temperature and appeared in one model: mean normalized difference vegetation index (NDVI), area-weighted mean of shape index (SHAPE_AM) for tree canopy, and largest patch index (LPI) for tree canopy. Lastly, total class area (CA) for buildings appeared in one multiple regression; it was positively associated with mean ambient night temperature but exhibited only marginal statistical significance.

The GWR analysis maintained each multiple regression's fitness established during the preceding global OLS technique, and corroborated inferential findings across those six models. It is

Table 3
Geographically weighted regression (GWR) parameter estimates for multiple regressions between-significant landscape predictors- and average ambient night time temperature across 34 New York City streetscapes.
[Independent model variables have been transformed to meet normality, and standardized to set the mean at 0 and variance equal to 1.].

Statistical measures and independent variables	Models					
Diagnostic Statistics	Model 1	Model 2	Model 3	Model 4	Model 5	Model 6
Akaike's Information Criterion (AICc)	28.084	29.592	40.717	42.734	43.933	44.934
R-Square	0.741	0.703	0.715	0.653	0.675	0.662
Adaptive Kernel Neighbors	90.000%	90.000%	53.636%	83.075%	59.418%	61.211%
Sigma	0.103	0.114	0.127	0.146	0.142	0.147
Effective Number Parameters	4.564	3.474	7.239	6.026	6.989	6.884
F	23.663	29.272	10.776	10.473	9.38	9.013
Model *P*-value	<0.001	<0.001	<0.001	<0.001	<0.001	<0.001
Residuals Global Moran's *I* z-score	−0.807 §	−0.315 §	1.128 §	0.815 §	0.971 §	1.003 §
Local Regression Parameter Descriptive Statistics: (Median)						
Constant	14.908	14.912	14.965	14.928	14.963	14.955
LiDAR derived metric †						
Mean elevation	−0.254	−0.251	−0.154	−0.213	−0.200	−0.284
Urban chasm cross section ‡						
Sky-view factor	−0.372	−0.389	–	–	–	–
Planimetric derived metric ‡						
Mean building height	–	–	0.168	0.299	0.244	0.200
Tree canopy class configuration ‡						
Area-weighted mean of shape index (SHAPE_AM)	–	–	–	−0.205	–	–
Largest patch index (LPI)	–	–	–	–	−0.176	–
Buildings class configuration ‡						
Total class area (CA)	–	–	–	–	–	0.111
Roads class configuration ‡						
Landscape shape index (LSI)	0.098	–	0.212	0.230	0.200	0.194
Photosynthesis activity ‡						
Mean normalized difference vegetation index (NDVI)	–	–	−0.191	–	–	–

Symbol designations: † Light Detection and Ranging (LiDAR) data has 0.3048 m (1 ft) pixel resolution; ‡ associated variables calculated for a 250-m radius streetscape from its corresponding temperature sample site; § spatial pattern of residuals was statistically random based on established distance of 8 km, and dash, –, indicate no statistically significant relationship observed.
Technical notes: Landscape ecology metrics computed based on land cover data with 0.9144 m (3 ft) pixel resolution (NYC, 2015), and using queen contiguity (8-neighbor rule); search area for isolation/proximity metrics was 20 m; edge depth for core area calculations was 5 m.

important to note, when using local regression modeling methods, which covariates had spatial autocorrelation. Of the eight explanatory variables previously employed across the six multiple regression models, only total class area (CA) for buildings was spatially random. Seven independent streetscape predictors, and the dependent variable mean ambient night temperature, were spatially autocorrelated based on the foregoing Global Moran's *I*-test. The six GWR models explained between 65% and 74% of the variation of mean ambient night temperature (Table 3). Based on AICc values, the GWR models maintained the same ranking with Model 1 being best-fitting (AICc = 28.08) and increasing to Model 6 as the worst-fitting (AICc = 44.93). From the adaptive kernel selection technique, the percentage (number) of neighbors used in the GWR models ranged from 53.64% (18) for Model 3−90% (31) for Models 1 and 2; furthermore, Models 4, 5, and 6 integrated 83.08% (28), 59.42% (20), and 61.21% (21) neighbors, respectively. The standardized partial coefficients (median values) of the GWR models corroborated covariate directionality established in the OLS models. Lastly, the six GWR models remediated errors possibly caused by spatial autocorrelation of input variables, as publicized by independence of residuals from the Global Moran's *I*-test.

A key advantage of GWR is that spatial variability in model parameters can be illustrated to help explain inferential relationships through geographical study (Shaker et al., 2017). Using negative and positive 1.65 ($\alpha = 0.10$) as the upper and lower bounds for the pseudo-*t*-statistics, maps were created to illustrate local relationships between-natural and built streetscape characteristics- and mean ambient night temperature for Model 3 (Fig. 7). Directionality and relative strength of relationships were presented using the estimated standardized coefficients; albeit, local areas of non-statistical significance were masked out using the aforementioned pseudo-*t*-statistics upper and lower limits. Along with the local covariates, local R^2 values and the local standardized residuals were illustrated for Model 3 from the GWR evaluation. Unlike OLS, the spatial pattern of GWR's coefficient of determination (R^2) displayed local variation; additionally, Model 3 had local R^2 values from 0.36 in the south ascending to 0.71 in the north. Model 3 used two negative and two positive streetscape characteristics for locally explaining mean ambient night temperature across the study area. Based on the pattern of local covariates, mean NDVI had the largest significant distribution and strongest negative influence on mean night temperature. Mean NDVI is important for decreasing the UHI across the study area, other than an area of insignificance in the southwest. Mean elevation was the other negative predictor of mean night temperature for Model 3; however, the southern half of the study area was locally statistically insignificant as illustrated by the pseudo-*t*-statistics. Based on the pattern of local covariates, LSI for roads had the largest significant distribution and strongest positive influence on mean night temperature. Mean building height was the other positive predictor of mean night temperature for Model 3; however, a region in the southern part of the study area was locally statistically insignificant as shown by the pseudo-*t*-statistics. The results suggest that local covariate significance is impacted by their synergistic effect on overall model fitness, thus caution should be taken when interpreting local multivariate inference. That said, GWR adjusts for spatially autocorrelated variables, allows for local illustration of model predictors, and should be considered during future UHI studies.

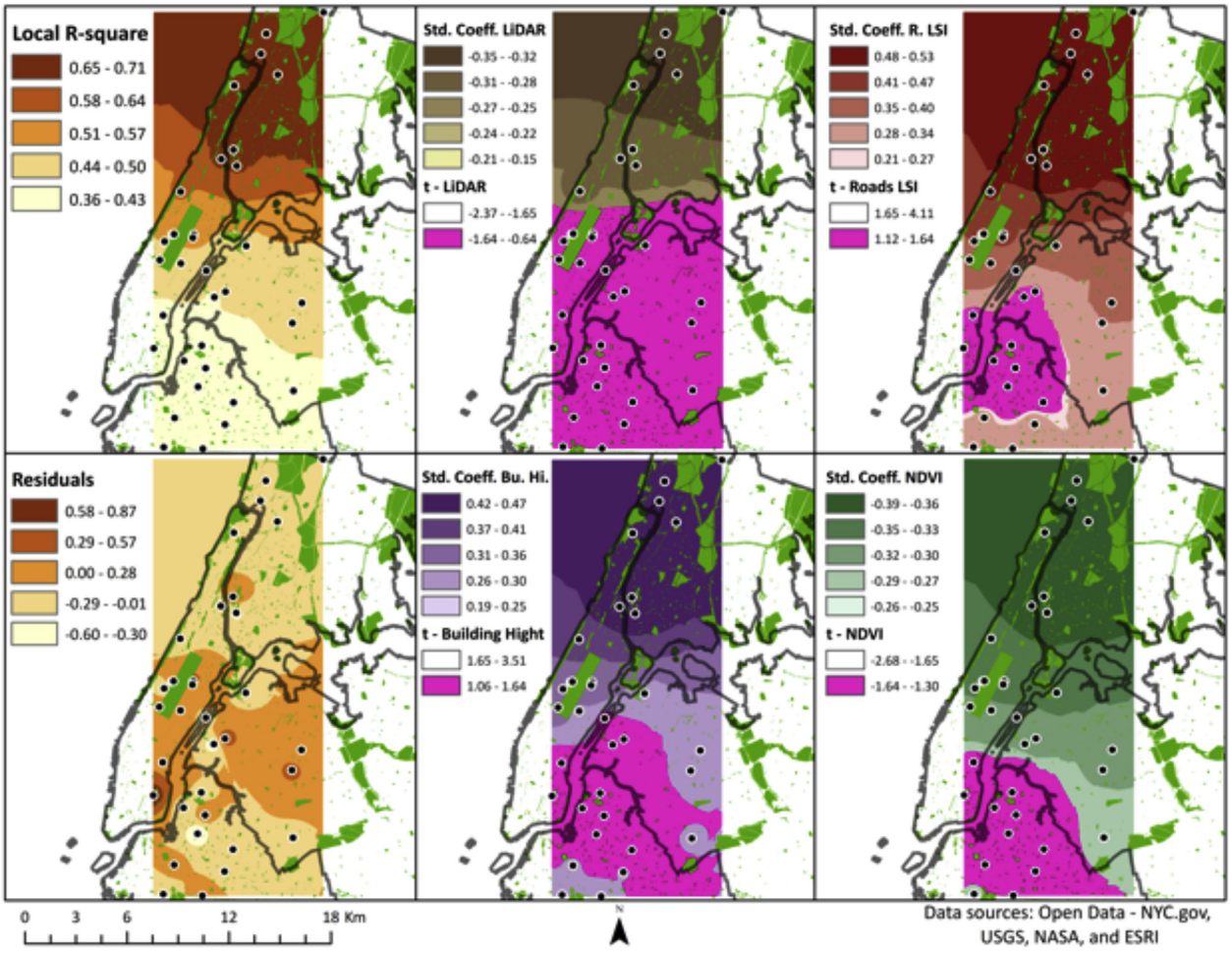

Fig. 7. Local R^2 and standardized residuals of the geographically weighted regression (GWR) Model 3 (Table 3); statistically significant spatial patterns of GWR local covariates for streetscape predictors. Magenta coloring masks out areas of local non-statistical significance using pseudo-*t*-values ($\alpha = 0.10$). Interpolated surfaces were created using inverse distance weighting (IDW).

4.4. Collinearity assessment of key streetscape predictors

From the foregoing bivariate and multiple regression analyses, 14 predictors of mean ambient night temperature were assessed for collinearity *ex post facto* using a two-tailed Pearson correlation matrix (Table 4). Between the 14 variables, 34 bivariate relationships recorded statistical significance above the 95% confidence level and 44 correlations were above the 90% confidence level.

Table 4
Pearson product-moment correlation coefficients (two-tailed) matrix of the 14 most relevant statistically significant streetscape predictors of mean ambient night temperature ($N = 34$).

UHI predictor	14	13	12	11	10	9	8	7	6	5	4	3	2	1
Description	R.LSI	R.FRAC	R.SHAPE	B.COHE.	B.CA	% Build	T.LPI	T.CORE	T.SHAPE	% Tree	NDVI	B.Height	SVF	LiDAR
(1) LiDAR mean elevation	−0.01	−0.53[a]	−0.55[a]	−0.27	−0.13	−0.10	0.47[a]	0.45[a]	0.43[b]	0.55[a]	0.54[a]	0.04	0.14	1
(2) Sky-view factor (SVF)	−0.18	−0.25	−0.21	−0.43[b]	−0.65[a]	−0.66[a]	0.29	0.29	0.30	0.31	0.51[a]	−0.41[b]	1	
(3) Mean building height	−0.40[b]	−0.11	−0.15	0.66[a]	0.09	0.11	0.32	0.29	0.36[b]	0.25	−0.09	1		
(4) Mean NDVI	0.05	−0.43[b]	−0.41[b]	−0.17	−0.44[a]	−0.56[a]	0.74[a]	0.72[a]	0.75[a]	0.80[a]	1			
(5) Percent tree canopy	−0.13	−0.60[a]	−0.63[a]	0.00	−0.47[a]	−0.53[a]	0.85[a]	0.79[a]	0.88[a]	1				
(6) Tree SHAPE_AM	−0.20	−0.38[b]	−0.38[b]	0.15	−0.49[a]	−0.59[a]	0.98[a]	0.96[a]	1					
(7) Tree CORE_AM	−0.18	−0.28	−0.27	0.09	−0.48[a]	−0.58[a]	0.99[a]	1						
(8) Tree LPI	−0.20	−0.34	−0.34	0.09	−0.49[a]	−0.58[a]	1							
(9) Percent buildings	0.10	0.09	0.60	0.29	0.96[a]	1								
(10) Buidings CA	0.20	0.15	0.14	0.39[b]	1									
(11) Buildings COHESION	−0.30	0.10	0.10	1										
(12) Roads SHAPE_AM	0.37[b]	0.98[a]	1											
(13) Roads FRAC_AM	0.39[b]	1												
(14) Roads LSI	1													

[a] Correlation is significant at the 0.01 level.
[b] Correlation is significant at the 0.05 level.

Focusing on the "very" category established in the methods, eight natural and built streetscape characteristics recorded nine very positive (>0.75) coefficients; albeit no negative correlation coefficients (<−0.75) were recorded at this statistical strength. With four scores recorded, percent tree canopy exhibited the highest degree of collinearity across the 14 predictors. SHAPE_AM for tree canopy, LPI for tree canopy, and CORE_AM for tree canopy all recorded three very positive scores. Percent buildings, CA for buildings, FRAC_AM for roads, and SHAPE_AM for roads all recorded one very positive coefficient with another predictor. Note the eight streetscape characteristics only conveyed a high degree of collinearity with predictors of the same land cover class. Correlation among landscape measures, especially class configuration metrics of the same land cover type, can be expected since they capture some aspect of the landscape mosaic. Although numerically these streetscape predictors appear redundant, their definitions and interpretations can render different explanations. Therefore, researchers should use caution when removing predictors prior to investigating their singular and synergistic relationships with phenomena under study. For this study, the methodological sequence decreased information loss and optimized UHI knowledge within a complex urban ecosystem.

5. Discussion

5.1. Importance of streetscape predictors

Accurately predicting patterns of urban heat island (UHI) demands knowledge of how natural and human-created landscapes change weather and climate across spatial and temporal scales. The streetscape characteristics associated with increased UHI-related night temperature in New York City (NYC) were linked to both natural and built causes. Across the modeling techniques used in this study, human-built streetscape features were found to be drastically more important than natural features for predicting mean ambient night temperature. Before delving deeper, it is important to point out very few landscape features or climate-related variables remain untouched by humanity. From greenhouse gas emissions influencing global climate change, weather patterns, and sea-level rise, to centuries of re-urbanization in major urban area, megacities such as NYC have very few biogeochemical systems that are natural. Of course, natural predictors play an important role in modeling and understanding the synergistic effects the urban ecosystem has on UHI. That said, besides elevation, this study's results highlighted the importance of photosynthesis activity and configuration and composition of tree canopy for reducing UHI. The negative correlation between percent tree canopy and mean ambient night temperature was expected, and this finding follows the general cooling effects associated with canopy shading, leaf reflectance, and evapotranspiration. The stronger negative correlation between mean normalized difference vegetation index (NDVI) and mean ambient night temperature was also expected, since higher NDVI values signify healthier vegetation, improved photosynthesis, and fuller leaf canopies. Important research remains on how to maximize NDVI values in urban ecosystems, but the literature suggests increasing native species (flora and fauna) richness, complexity, and diversity. Since landscape compositions lack detailed information needed by engineers, architects, urban planners and designers to create solutions in complex urban settings (Leitão et al., 2012) configuration metrics were utilized. Area-weighted mean shape index (SHAPE_AM) for trees was negatively correlated with mean ambient night temperature. As this class metric increases tree canopy patches become more irregular shaped, in comparison to one single maximally compact tree canopy (i.e., almost square) patch (McGarigal et al., 2012), and

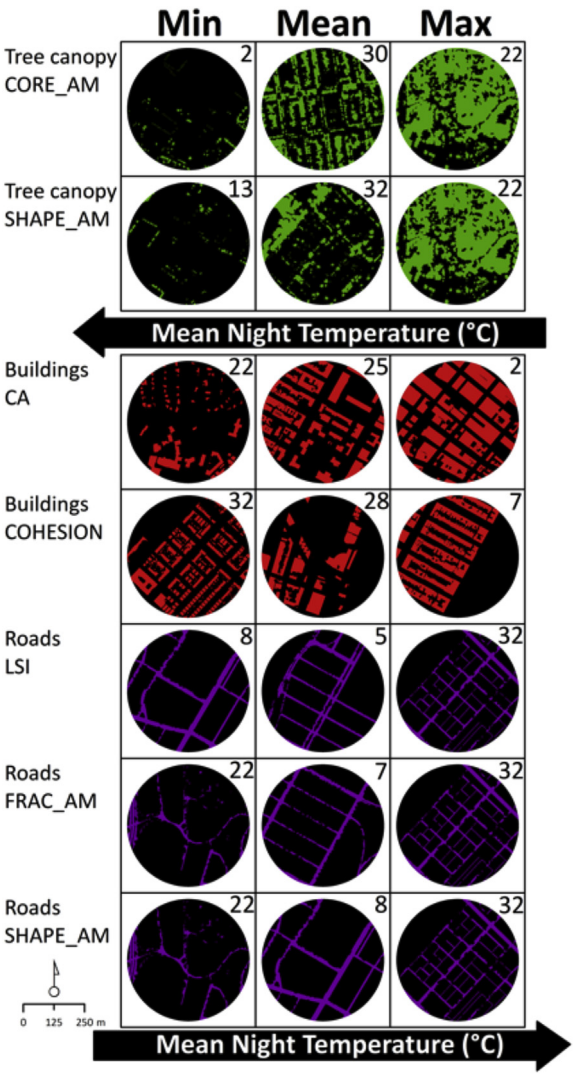

Fig. 8. Key land cover class configuration metrics illustrating relationships between streetscape design and mean ambient night temperature. Identification numbers correspond to sample site locations in Fig. 1.

the UHI effect decreases. Lastly, the landscape ecology class metrics provided valuable insight for naturally decreasing the UHI (Fig. 8), such as using strategic tree plantings to fill canopy gaps to increase core areas (CORE_AM) and increase their patch shape complexity (SHAPE_AM). Given very high economic value of available free ground in megacities like NYC, retrofitting existing buildings with green screening and green rooftops will accomplish large-scale UHI mitigation designs (Santamouris, 2014).

Built streetscape characteristics capturing building and road morphology were the most dominant predictors of UHI across the NYC sample sites. From the modeling techniques used, the most important streetscape predictors of mean ambient night temperature were building class and road class configuration. Specifically, two buildings configuration metrics consistently correlated with ambient night temperature: (*i*) total class area (CA) and (*ii*) patch cohesion index (COHESION). Akin to landscape compositions, CA is a measure of landscape composition and provides limited information useful for creating urban design strategies for sustainable development planning purposes (Leitão et al., 2012). Conversely, COHESION for buildings provides detailed urban design information and correspond with a previously established relationship

between urban COHESION and ecological well-being at the country scale (Shaker, 2015). This is important to note, as a fertile area of research remains for understanding if local landscape patterns maintain the same effect on processes across spatial scales (Greene and Kedron, 2018). The positive relationship between COHESION and mean ambient night temperature signifies that when buildings are less sub-divided and more physically connected there is greater UHI effect. Paired with the positive relationships between night temperature, CA, and mean building height, this information suggests urban planners, designers, and engineers should create streetscapes that include smaller building footprint areas, which are of shorter heights, and that are dispersed from each other. Indeed, new research is needed for assessing tradeoffs between per capita energy use in buildings and the heat generated by the buildings themselves, which would help optimize structural design at specific geography.

The following three noteworthy road configuration metrics correlated with ambient night temperature: (*i*) area-weighted mean of fractal area dimension (FRAC_AM), (*ii*) landscape shape index (LSI), and (*iii*) area-weighted mean shape index (SHAPE_AM). FRAC_AM values range between 1 and 2, and as the class metric increases so does road shape complexity across a range of spatial scales (patch sizes) within a landscape; FRAC approaches 1 for shapes with very simple perimeters (i.e., squares), and approaches 2 for shapes with highly convoluted, plane-filling perimeters (McGarigal et al., 2012). The positive correlation between FRAC_AM and mean ambient night temperature suggests that roads with very simple perimeters (i.e., squares) are better for dissipating thermal energy associated with UHI. LSI values are greater than or equal to 1, and as this class metric increases without limit road patches become more separated; LSI equal 1 when the streetscape consists of a single maximally compact road (i.e., almost square) patch (McGarigal et al., 2012). The positive correlation between LSI and mean ambient night temperature suggests that streetscapes with fewer amassed roads are better for dissipated thermal energy associated with UHI then many disaggregated roads. Albeit numerically cross-correlated with FRAC_AM (Table 4), SHAPE_AM also recorded a positive correlation with mean ambient night temperature. SHAPE_AM values record 1 or greater without limit, and as this class metric increases the road patches become more irregular shaped; SHAPE_AM equal 1 when the streetscape consists of a single maximally compact road (i.e., almost square) patch (McGarigal et al., 2012). These combined findings are novel and suggest that larger roads-which are fewer, wider, straighter, have more traffic, and faster traffic speeds-in streetscapes dissipate thermal energy associated with UHI. Not accepting road configuration to be spurious, erroneous findings may come from 'top-down' remote sensing viewpoints in which tree canopy over hang other landscape characteristics. Thus, corroborating studies with 'bottom-up' approaches and datasets with 'leaf-off' or non-remote sensed data should quickly follow. Lastly, research gaps remain for investigating how transportation influences thermal heating (i.e., engine exhaust), cooling (i.e., automobiles vs road albedo), and mixing (i.e., traffic speed) in cities.

5.2. Urban resilience planning and design

Cities and their urban populations are exacerbating climate change, ultimately degrading their local to global life-supporting ecosystems. While the prospects of urbanization extensively change depending on the status quo of society (Ahern, 2013), economy, and environment, current landscape changes brought by extra-anthropogenic factors such as climate change and sea-level rise, make adequate design and management of cities additionally relevant (Goudie, 2018). Management of solar radiation, exposure, and the sheer occupation of urban fabric itself, must be seen within the sustainability paradigm, embedding the integration of city planning, policy-making and stakeholders as to allow cities to become cohesively sustainable, beyond the urban fabric itself, and in lieu of the coherence of its design and sustainable form. Solutions for heat mitigating land features, such as the occupation of green facades (Pérez et al., 2017) and urban farms (Ackerman et al., 2014), should (and frequently in modern developed cities are) become an integral part of urban environments. Surely the leading economies and innovation found in megacities will allow them to lead the way in urban resilience, sustainable development planning, and innovative design.

Under the tests of population growth, urbanization, and future climate changes, need continues for sustainable mitigation and adaptation strategies for UHI effect. The rapid and dramatic changes of urban cores both in the developing and developed world, call for methods that highlight beyond the traditional vision of urban areas. It is the integration of novel methods found in spatial sciences, where one can address the complexity of infrastructural challenges together with the cohesive nature of the urban form (Vaz, 2016). While the problems in the developed and developing world are intrinsically different within the anthroposphere, it is the vision of integrating tools found in quantitative spatial sciences that can offer the best solutions given the recent advances of (*i*) high-resolution imagery, (*ii*) capacity of data repository and their historic inventories, as well as (*iii*) data retrieval and computation. To use spatial and sustainability sciences to further understand urban metabolism, where the intricate urban fabric, energy efficiency, environmental integrity, social equity, and economic growth must be improved to achieve greater resilience in cities and regions (Baccini, 1996; Carreón and Worrell, 2018). Inspection of urban heat islands, such as proposed in this study for New York, poses a novel approach to detailed spatial analytics, forwarding elegant planning and design solutions for the larger body of spatial decision support systems (Coutinho-Rodrigues et al., 2011; Lombardi et al., 2017).

An important yet often unexplored research topic is the spatial patterns of future urban development and its impacts (Güneralp et al., 2017). With the significant advances of geospatial technologies, the study of landscape and land use has become an increasingly refined endeavor (Kushwaha and Mukhopadhyay, 2013). The necessary push from planning and policymakers to assess land use change (Olawumi and Chan, 2018) and deterministically understand the impacts on land cover (Vaz et al., 2012), make in the context of streetscape characteristics fundamental to understand spatial heterogeneity as well as enhance microscale and mesoscale modeling applications within urban climate dynamics. From an economic standpoint, it is the friction of socio-economic vetted interests that often contradict sustainable development (Lélé, 1991), which may lead to strenuous interactions between urban cores and their supporting particularities in rapidly changing cities (Arsanjani et al., 2013). Having a rigorous quantification of the fine-grained spatial scale (Zambon et al., 2018) may provide a more holistic understanding of the topologic relations of spatial-urban interactions (Turner et al., 1989), ultimately leading to more functional cities (Grimm et al., 2008; Pickett et al., 2011). Streetscape predictors should examine the compounds of the complexity of heat factors, as to reconsider in the planning structure the integration for well-being that should be implicit in any sustainable city (Spokane et al., 2007). Beyond streetscape metrics lies thus the potential to integrate smarter energy usage of urban regions, while considering the multi-tiered complexity brought by the juggling aspects of built-environment, road networks, and the panoply of actors within the urban ecosystem.

6. Conclusions

Cities experience the urban heat island (UHI), which continue to pose challenges for humanity's increasingly urban population. The NYC Panel on Climate Change (NYCPCC, 2015) announced that its growing city is becoming increasingly vulnerable to sea level rise, can expect increased precipitation and coastal flooding, and will likely experience more frequent and intense heat waves. In response, PlaNYC (NYC, 2007) was launched in 2007 as a long-range economic and environmental sustainability plan incorporating ten policy areas. In 2015 PlaNYC transitioned to OneNYC (NYC, 2015) with the ambitious goal of making NYC the most resilient, equitable, and sustainable city in the world. Although development progress has been made through these initiates (NYC, 2018), work remains for scientists to help NYC prepare for a warming world (Rosenzweig et al., 2010). As such, this paper adds to the UHI, urban sustainable, planning and design literature in several ways by fulfilling its three guiding objectives. It began by using the rarely assessed but most ideal urban canopy layer (UCL) temperature data to illustrate NYC's UHI and to evaluate natural and built streetscape characteristics. Next, one of the most detailed (0.914 m resolution) and accurate (96%) land cover data set available was used for capturing landscape composition, configuration, and diversity; furthermore, assessing a more complete set of landscape predictors never before seen in one UHI study. In UHI context, it showcased rarely used spatial analysis methods sensitive to spatial autocorrelation for corroborating traditional global (without spatial reference) statistical techniques. Lastly, this study provided novel and informative results from freely available temperature and landscape data.

Streetscapes are highly couple socio-ecological systems, which need new approaches and understanding for establishing sustainable urbanization. First, in order to assess the spatial pattern of mean ambient night temperature across 34 streetscapes in NYC, global and local statistical methods were employed. Specifically, a Paired Sample T-Test determined that there was a significant difference between the coldest and warmest night temperature locations. Global Moran's *I*-test corroborated spatial autocorrelation of mean night temperature, as with many of the natural and built streetscape predictors. To illustrate NYC's UHI across the study area, ordinary kriging was used to interpolate a predicted surface of UCL temperatures recorded across 34 weather stations, and Local Getis-Ord Gi* (Getis and Ord, 1992) was used to map statistically significant "hot spots" and "cold spots" of those data. Second, various inferential statistical models were established to uncover which of the 90 + natural and built streetscape characteristics were most capable of predicting mean ambient night temperature. Specifically, Pearson's correlation test (*r*), ordinary least squares (OLS) regression, and geographically weighted regression (GWR) were used as modeling tools for this study. Although spatial autocorrelation was reported and corrected for, the inferential relationships between-natural and built streetscape characteristics- and mean ambient night temperature held true across all methods. Global inferential tests revealed that sky-view factor, photosynthesis activity, elevation, and road configuration were the strongest predictors of mean ambient night temperature. Six multiple regression models were ultimately made, with GWR fitting the UHI aptly ($R^2 = 65–74\%$). Third, GWR was used to illustrate and evaluate local patterns of correlated associations from a key model with four key explanatory variables. Pointedly, important explanatory covariates were illustrated using local pseudo-*t* statistics and linked to mean ambient night temperature, supporting the importance of GWR for understanding local UHI interactions. Although the GWR findings cannot be assigned to other geographic locations, the corroborating inferential findings can be related to streetscapes of similar geography, climate, and urban morphology.

Eliminating UHI is requisite for creating urban sustainability. NYC has a strong foundation for urban sustainability, with original "seers" such as William Whyte, Jane Jacob, and Ian McHarg all using it as their living-laboratory to create more habitable and sustainable cities (McPhearson, 2011). That said, UHI is the reason of roughly 1/3 of entire warming NYC has experienced during the 20th century (Gaffin et al., 2008), and much work remains for remediating this anthropogenic climate alteration. In order to create resilient and sustainable cities it is important to not be one dimension, to be mindful of tradeoffs and synergies that occur when optimizing coupled human-environmental systems. In this regard, Meerow and Newell (2017) suggested using stakeholder-weighted spatial planning of green infrastructure that combine six advantages: 1) air quality; 2) green space; 3) landscape connectivity; 4) social vulnerability; 5) stormwater management; and 6) urban heat island amelioration. Although "ecological land-use complementation" (Colding, 2007) is central for restoring ecosystem processes essential for supporting biodiversity, such as connecting greenspace across urban parks and rooftops, much remains for engineers, architects, urban planners and designers to create multidimensional solutions that address all three spheres of sustainability (economic growth, social equity, environmental integrity) in complex urban settings. Fortunately, the results confirm that landscape configuration metrics are stronger predictors of mean ambient night temperature than composition measures, which provide detailed information useful to practitioners for remediating negative effects associated with UHI. Streetscape design, particularly road patterns and process, requires more consideration when attempting to mitigate UHI during future sustainability planning, urban renewal projects, and research. That said, data sets and research tools are likely not the preventive factors for advancing cities toward their sustainable urbanization goals. Rather it is conflicting governance of increasingly vulnerable growing populations within geographically restricted, dense, overpopulated urban environments. By exploring UHI in NYC, and its correlations with many built and natural streetscape characteristics, applied insight useful for improving urban ecological integrity, resilience and sustainable urbanization was made. In sum, studies like this one help to provide cities empirically supported planning and design strategies for moving humanity closer to destination sustainability.

Acknowledgments

Binghamton University (SUNY) and Ryerson University provided financial support for this research. Daphne Shaker and Lydia Shaker of GeoEco Design (Syracuse, NY) and Jase Bernhardt of Hofstra University (Hempstead, NY) gave constructive comments on earlier versions of this manuscript. The authors declare no conflict of interest.

Appendix A. Supplementary data

Supplementary data to this article can be found online at https://doi.org/10.1016/j.jclepro.2019.05.389.

References

Diniz-Filho, J.A.F., Rangel, T.F.L., Bini, L.M., 2008. Model selection and information theory in geographical ecology. Glob. Ecol. Biogeogr. 17 (4), 479–488.
Ackerman, K., Conard, M., Culligan, P., Plunz, R., Sutto, M.P., Whittinghill, L., 2014. Sustainable food systems for future cities: the potential of urban agriculture. Econ. Soc. Rev. 45 (2), 189–206. Summer.
Ahern, J., 2013. Urban landscape sustainability and resilience: the promise and challenges of integrating ecology with urban planning and design. Landsc. Ecol.

28 (6), 1203–1212.
Akaike, H., 1978. A Bayesian analysis of the minimum AIC procedure. Ann. Inst. Stat. Math. 30, 9–14. Part A.
Akbari, H., Pomerantz, M., Taha, H., 2001. Cool surfaces and shade trees to reduce energy use and improve air quality in urban areas. Sol. Energy 70 (3), 295–310.
Alberti, M., 2008. Advances In Urban Ecology: Integrating Humans and Ecological Processes in Urban Ecosystems. Springer, New York (NY).
An, S.M., Kim, B.S., Lee, H.Y., Kim, C.H., Yi, C.Y., Eum, J.H., Woo, J.H., 2014. Three-dimensional point cloud based sky view factor analysis in complex urban settings. Int. J. Climatol. 34 (8), 2685–2701.
Arnfield, A.J., 2003. Two decades of urban climate research: a review of turbulence, exchanges of energy and water, and the urban heat island. Int. J. Climatol. 23 (1), 1–26.
Arsanjani, J.J., Helbich, M., de Noronha Vaz, E., 2013. Spatiotemporal simulation of urban growth patterns using agent-based modeling: the case of Tehran. Cities 32, 33–42.
Baccini, P., 1996. Understanding regional metabolism for a sustainable development of urban systems. Environ. Sci. Pollut. Res. 3 (2), 108–111.
Balchin, W.G.V., Pye, N., 1947. A micro-climatological investigation of Bath and the surrounding district. Quart. J. Roy. Meteor. Soc. 73, 297–323.
Batty, M., 2008. The size, scale, and shape of cities. science 319 (5864), 769–771.
Batty, M., 2011. When all the world's a city. Environ. Plan. 43 (4), 765–772.
Berardi, U., GhaffarianHoseini, A., GhaffarianHoseini, A., 2014. State-of-the-art analysis of the environmental benefits of green roofs. Appl. Energy 115, 411–428.
Bornstein, R., LeRoy, M., 1990. Urban barrier effects on convective and frontal thunderstorms. Preprint volume. In: Fourth AMS Conference on Mesoscale Processes. Boulder, CO, 25-29 June.
Bornstein, R., Lin, Q., 2000. Urban heat islands and summertime convective thunderstorms in Atlanta: three case studies. Atmos. Environ. 34 (3), 507–516.
Bowler, D.E., Buyung-Ali, L., Knight, T.M., Pullin, A.S., 2010. Urban greening to cool towns and cities: a systematic review of the empirical evidence. Landsc. Urban Plan. 97 (3), 147–155.
Burnham, K.P., Anderson, D.R., 2003. Model Selection and Multimodel Inference: a Practical Information-Theoretic Approach. Springer Science & Business Media.
Buyantuyev, A., Wu, J., 2010. Urban heat islands and landscape heterogeneity: linking spatiotemporal variations in surface temperatures to land-cover and socioeconomic patterns. Landsc. Ecol. 25 (1), 17–33.
Carpenter, S.R., Mooney, H.A., Agard, J., Capistrano, D., DeFries, R.S., Díaz, S., et al., 2009. Science for managing ecosystem services: beyond the Millennium Ecosystem Assessment. Proc. Natl. Acad. Sci. Unit. States Am. 106 (5), 1305–1312.
Carreón, J.R., Worrell, E., 2018. Urban energy systems within the transition to sustainable development. A research agenda for urban metabolism. Resour. Conserv. Recycl. 132, 258–266.
Ceballos, G., Ehrlich, P.R., Dirzo, R., 2017. Biological annihilation via the ongoing sixth mass extinction signaled by vertebrate population losses and declines. Proc. Natl. Acad. Sci. Unit. States Am. 114 (30), E6089–E6096.
Colding, J., 2007. 'Ecological land-use complementation' for building resilience in urban ecosystems. Landsc. Urban Plan. 81 (1–2), 46–55.
Connors, J.P., Galletti, C.S., Chow, W.T., 2013. Landscape configuration and urban heat island effects: assessing the relationship between landscape characteristics and land surface temperature in Phoenix, Arizona. Landsc. Ecol. 28 (2), 271–283.
Coutinho-Rodrigues, J., Simão, A., Antunes, C.H., 2011. A GIS-based multicriteria spatial decision support system for planning urban infrastructures. Decis. Support Syst. 51 (3), 720–726.
Coutts, A.M., Tapper, N.J., Beringer, J., Loughnan, M., Demuzere, M., 2013. Watering our cities: the capacity for water sensitive urban design to support urban cooling and improve human thermal comfort in the Australian context. Prog. Phys. Geogr. 37 (1), 2–28.
Crane, P., Kinzig, A., 2005. Nature in the metropolis. Science 1225.
de Abreu-Harbich, L.V., Labaki, L.C., Matzarakis, A., 2015. Effect of tree planting design and tree species on human thermal comfort in the tropics. Landsc. Urban Plan. 138, 99–109.
de Morais, M.V.B., Marciotto, E.R., Guerrero, V.V.U., de Freitas, E.D., 2017. Effective albedo estimates for the Metropolitan Area of São Paulo using empirical sky-view factors. Urban Clim. 21, 183–194.
Debbage, N., 2013. Sky-view factor estimation: a case study of Athens, Georgia. Geogr. Bull. 54 (1), 49–57.
Deng, C., Wu, C., 2013. Examining the impacts of urban biophysical compositions on surface urban heat island: a spectral unmixing and thermal mixing approach. Remote Sens. Environ. 131, 262–274.
Dormann, C.F., McPherson, J.M., Araújo, M.B., Bivand, R., Bolliger, J., Carl, G., Davies, R.G., Hirzel, A., Jetz, W., Kissling, W.D., Kühn, I., et al., 2007. Methods to account for spatial autocorrelation in the analysis of species distributional data: a review. Ecography 30, 609–628.
Dormann, C.F., Elith, J., Bacher, S., Buchmann, C., Carl, G., Carré, G., Marquéz, J.R.G., Gruber, B., Lafourcade, B., Leitão, P.J., Münkemüller, T., McClean, C., Osborne, P.E., Reineking, B., Schröder, B., Skidmore, A.K., Zurell, D., Lautenbach, S., 2013. Collinearity: a review of methods to deal with it and a simulation study evaluating their performance. Ecography 36, 27–46. https://doi.org/10.1111/j.1600-0587.2012.07348.x.
Duneier, M., 2006. Ethnography, the ecological fallacy, and the 1995 Chicago heat wave. Am. Sociol. Rev. 71 (4), 679–688.
Dutton, A., Carlson, A.E., Long, A.J., Milne, G.A., Clark, P.U., DeConto, R., et al., 2015. Sea-level rise due to polar ice-sheet mass loss during past warm periods. Science 349 (6244), aaa4019.
Eliasson, I., 1996. Urban nocturnal temperatures, street geometry and land use. Atmos. Environ. 30, 379–392.
ESRI – Environmental Systems Research Institute, 2016. ArcGIS 10.4. Released 2016. Computer Software, Redlands, CA.
Foley, J.A., DeFries, R., Asner, G.P., Barford, C., Gordon, B., Carpenter, S.R., Chapin, F.S., Coe, M.T., Daily, G.C., Gibbs, H.K., Helkowski, J.H., Holloway, T., Howard, E.A., Kucharik, C.J., Monfreda, C., Patz, J.A., Prentice, I.C., Ramankutty, N., Snyder, P.K., 2005. Global consequences of land use. Science 309, 570–574.
Foody, G.M., 2003. Geographical weighting as a further refinement to regression modelling: an example focused on the NDVI–rainfall relationship. Remote Sens. Environ. 88 (3), 283–293.
Forman, R.T., Wu, J., 2016. Where to put the next billion people. Nature 537 (7622), 608–611.
Forsythe, K.W., Marvin, C.H., Valancius, C.J., Watt, J.P., Aversa, J.M., Swales, S.J., et al., 2016. Geovisualization of mercury contamination in Lake St. Clair sediments. J. Mar. Sci. Eng. 4 (1), 19.
Forsythe, K.W., Hare, C., Buckland, A.J., Shaker, R.R., Aversa, J.M., Swales, S.J., MacDonald, M.W., 2018. Assessing fine particulate matter concentrations and trends in southern Ontario, Canada, 2003–2012. AIMS Environ. Sci. 5 (1), 35–46.
Fotheringham, A.S., Brunsdon, C., Charlton, M., 2003. Geographically Weighted Regression: the Analysis of Spatially Varying Relationships. John Wiley & Sons, West Sussex, England.
Fotheringham, A.S., Brunsdon, C., Charlton, M., 2004. Quantitative Geography. Sage Publications, London, England.
Gaffin, S.R., Rosenzweig, C., Khanbilvardi, R., Parshall, L., Mahani, S., Glickman, H., Goldberg, R., Blake, R., Slosberg, R.B., Hillel, D., 2008. Variations in New York City's urban heat island strength over time and space. Theor. Appl. Climatol. 94, 1–11.
Gaffin, S.R., Khanbilvardi, R., Rosenzweig, C., 2009. Development of a green roof environmental monitoring and meteorological network in New York City. Sensors 9, 1–10.
Gal, T., Rzepa, M., Gromek, B., Unger, J., 2007. Comparison between sky view factor values computed by two different methods in an urban environment. Acta Climatol. Chorol. 40–41, 17–26.
Gedzelman, S.D., Austin, S., Cermak, R., Stefano, N., Partridge, S., Quesenberry, S., Robinson, D.A., 2003. Mesoscale aspects of the urban heat island around New York City. Theor. Appl. Climatol. 75 (1–2), 29–42.
Gerland, P., Raftery, A.E., Ševčíková, H., Li, N., Gu, D., Spoorenberg, T., et al., 2014. World population stabilization unlikely this century. Science 346 (6206), 234–237.
Getis, A., Ord, J.K., 1992. The analysis of spatial association by use of distance statistics. Geogr. Anal. 24 (3), 189–206.
Gill, S.E., Handley, J.F., Ennos, A.R., Pauleit, S., 2007. Adapting cities for climate change: the role of the green infrastructure. Built. Environ. 33 (1), 115–133.
Goudie, A.S., 2018. Human Impact on the Natural Environment. John Wiley & Sons.
Greene, C.S., Kedron, P.J., 2018. Beyond fractional coverage: a multilevel approach to analyzing the impact of urban tree canopy structure on surface urban heat islands. Appl. Geogr. 95, 45–53.
Grimm, N.B., Faeth, S.H., Golubiewski, N.E., Redman, C.L., Wu, J., Bai, X., Briggs, J.M., 2008. Global change and the ecology of cities. Science 319 (5864), 756–760.
Grimmond, C.S.B., Potter, S., Zutter, H., Souch, C., 2001. Rapid methods to estimate sky- view factors applied to urban areas. Int. J. Climatol. 21, 903–913.
Guhathakurta, S., Gober, P., 2007. The impact of the Phoenix urban heat island on residential water use. J. Am. Plan. Assoc. 73 (3), 317–329.
Güneralp, Burak, Zhou, Yuyu, Ürge-Vorsatz, Diana, Gupta, Mukesh, Yu, Sha, Patel, Pralit L., Fragkias, Michail, Li, Xiaoma, Karen, C., Seto, 2017. Global scenarios of urban density and its impacts on building energy use through 2050. Proc. Natl. Acad. Sci. Unit. States Am. 114 (34), 8945–8950.
Hamstead, Z.A., Kremer, P., Larondelle, N., McPhearson, T., Haase, D., 2016. Classification of the heterogeneous structure of urban landscapes (STURLA) as an indicator of landscape function applied to surface temperature in New York City. Ecol. Indicat. 70, 574–585.
Ivajnšič, D., Kaligarič, M., Žiberna, I., 2014. Geographically weighted regression of the urban heat island of a small city. Appl. Geogr. 53, 341–353.
Jahani, B., Mohammadi, B., 2018. A comparison between the application of empirical and ANN methods for estimation of daily global solar radiation in Iran. Theor. Appl. Climatol. 1–13. https://doi.org/10.1007/s00704-018-2666-3.
Jenerette, G.D., Harlan, S.L., Buyantuev, A., Stefanov, W.L., Declet-Barreto, J., Ruddell, B.L., et al., 2016. Micro-scale urban surface temperatures are related to land-cover features and residential heat related health impacts in Phoenix, AZ USA. Landsc. Ecol. 31 (4), 745–760.
Jim, C.Y., 2014. Air-conditioning energy consumption due to green roofs with different building thermal insulation. Appl. Energy 128, 49–59.
Jim, C.Y., Lo, A.Y., Byrne, J.A., 2015. Charting the green and climate-adaptive city. Landsc. Urban Plan. 138, 51–53.
Karlessi, T., Santamouris, M., Apostolakis, K., Synnefa, A., Livada, I., 2009. Development and testing of thermochromic coatings for buildings and urban structures. Sol. Energy 83 (4), 538–551.
Klenk, J., Becker, C., Rapp, K., 2010. Heat-related mortality in residents of nursing homes. Age Ageing 39 (2), 245–252.
Klinenberg, E., 2015. Heat Wave: A Social Autopsy of Disaster in Chicago. University

of Chicago Press.
Kolokotroni, M., Zhang, Y., Watkins, R., 2007. The London heat island and building coolingdesign. Sol. Energy 81 (1), 102–110.
Kong, F., Yin, H., James, P., Hutyra, L.R., He, H.S., 2014. Effects of spatial pattern of greenspace on urban cooling in a large metropolitan area of eastern China. Landsc. Urban Plan. 128, 35–47.
Kupfer, J.A., Farris, C.A., 2007. Incorporating spatial non-stationarity of regression coefficients into predictive vegetation models. Landsc. Ecol. 22 (6), 837–852.
Kushwaha, S.P.S., Mukhopadhyay, S., 2013. Sustainable land use planning using geospatial technology. In: Knowledge Systems Of Societies For Adaptation And Mitigation Of Impacts Of Climate Change. Springer, Berlin, Heidelberg, pp. 465–476.
Leitão, A.B., Miller, J., Ahern, J., McGarigal, K., 2012. Measuring Landscapes: A Planner's Handbook. Island press.
Lélé, S.M., 1991. Sustainable development: a critical review. World Dev. 19 (6), 607–621.
Lennon, J.J., 2000. Red-shifts and red herrings in geographical ecology. Ecography 23, 101–113.
Li, W., Putra, S.Y., Yang, P.P., 2004. GIS Analysis for the Climatic Evaluation of 3D Urban Geometry – the Development of GIS Analytical Tools for Sky View Factor GISDECO Seminar.
Li, J., Song, C., Cao, L., Zhu, F., Meng, X., Wu, J., 2011. Impacts of landscape structure on surface urban heat islands: a case study of Shanghai, China. Remote Sens. Environ. 115 (12), 3249–3263.
Li, X.M., Zhou, W.Q., Ouyang, Z.Y., 2013. Relationship between land surface temperatureand spatial pattern of greenspace: what are the effects of spatial resolution? Landsc. Urban Plan. 114, 1–8.
Lichstein, J.W., Simons, T.R., Shriner, S.A., Franzreb, K.E., 2002. Spatial autocorrelation and autoregressive models in ecology. Ecol. Monogr. 72 (3), 445–463.
Liu, J., Dietz, T., Carpenter, S.R., Alberti, M., Folke, C., Moran, E., et al., 2007. Complexity of coupled human and natural systems. science 317 (5844), 1513–1516.
Lombardi, P., Abastante, F., Torabi Moghadam, S., Toniolo, J., 2017. Multicriteria spatial decision support systems for future urban energy retrofitting scenarios. Sustainability 9 (7), 1252.
MacFaden, S.W., O'Neil-Dunne, J.P., Royar, A.R., Lu, J.W., Rundle, A.G., 2012. High-resolution tree canopy mapping for New York City using LIDAR and object-based image analysis. J. Appl. Remote Sens. 6 (1), 063567.
McGarigal, K., Cushman, S.A., Ene, E., 2012. FRAGSTATS: spatial pattern analysis program for categorical maps. Computer software program produced by the authors at the Universityof Massachusetts, Amherst. [cited 2017 June 3]. http://www.umass.edu/landeco/research/fragstats/fragstats.
McPhearson, P.T., 2011. Toward a sustainable New York City: greening through urban forest restoration. In: Sustainability in America's Cities. Island Press, Washington, DC, pp. 181–203.
Meerow, S., Newell, J.P., 2017. Spatial planning for multifunctional green infrastructure: growing resilience in Detroit. Landsc. Urban Plan. 159, 62–75.
Meir, T., Orton, P.M., Pullen, J., Holt, T., Thompson, W.T., Arend, M.F., 2013. Forecasting the New York City urban heat island and sea breeze during extreme heat events. Weather Forecast. 28 (6), 1460–1477.
Middel, A., Lukasczyk, J., Maciejewski, R., Demuzere, M., Roth, M., 2018. Sky view factor footprints for urban climate modeling. Urban Clim. 25, 120–134.
Moran, P.A., 1950. Notes on continuous stochastic phenomena. Biometrika 37 (1/2), 17–23.
Myint, S.W., Wentz, E.A., Brazel, A.J., Quattrochi, D.A., 2013. The impact of distinct anthropogenic and vegetation features on urban warming. Landsc. Ecol. 28 (5), 959–978.
Nakaya, T., Charlton, M., Lewis, P., Brunsdon, C., Yao, J., Fotheringham, S., 2014. GWR4 user manual. GWR4: window application for geographically weighted regression modelling. https://geodacenter.asu.edu/drupal_files/gwr/GWR4manual.pdf.
NASA – National Aeronautics and Space Administration, 2017. Measuring Vegetation (NDVI & EVI) [cited 2017 June 3]. https://earthobservatory.nasa.gov/Features/MeasuringVegetation/measuring_vegetation_2.php.
Norton, B.A., Coutts, A.M., Livesley, S.J., Harris, R.J., Hunter, A.M., Williams, N.S., 2015. Planning for cooler cities: a framework to prioritise green infrastructure to mitigate high temperatures in urban landscapes. Landsc. Urban Plan. 134, 127–138.
NRCC – Northeast Regional Climate Center, 2018. Normal Average Temperatures: Annual (1981-2010). Cornell University. http://www.nrcc.cornell.edu/.
NYC – New York City, 2007. PlaNYC: A Greener, pp. 1–156 greater New York. New York.
NYC – New York City, 2015. OneNYC: One New York: the Plan for a Strong and Just City, pp. 1–354. New York.
NYC – New York City Open Data, 2017. Open Data for All New Yorkers [cited 2017 June 5]. https://opendata.cityofnewyork.us/.
NYC – New York City, 2018. OneNYC: Progress Report 2018, pp. 1–51. New York.
NYCPCC – New York City Panel on Climate Change, 2015. New York city Panel on climate change 2015 report executive summary. Ann. N. Y. Acad. Sci. 1336, 9–17.
NYCPR – New York City Parks and Recreation, 2010. NYC Open Data: Landcover Raster Data [cited 2015 June 5] Available from:https://data.cityofnewyork.us/Environment/Landcover-Raster-Data-2010-3ft-Resolution/9auy-76zt.
NYSG – New York State Gazetteer, 2010. United States Census Bureau [cited 2017 June 5]. https://data.ny.gov/.
Oke, T.R., 1976. The distinction between canopy and boundary-layer urban heat islands. Atmosphere 14 (4), 268–277.
Oke, T.R., 1981. Canyon geometry and the nocturnal urban heat island: comparison of scale model and field observations. J. Climatol. 1 (3), 237–254.
Oke, T.R., 1982. The energetic basis of the urban heat island. Q. J. R. Meteorol. Soc. 108 (455), 1–24.
Oke, T.R., 1988. Street design and urban canopy layer climate. Energy Build. 11 (1–3), 103–113.
Oke, T.R., 2002. Boundary Layer Climates. Routledge.
Olawumi, T.O., Chan, D.W., 2018. A scientometric review of global research on sustainability and sustainable development. J. Clean. Prod. 183, 231–250.
Pantavou, K., Theoharatos, G., Mavrakis, A., Santamouris, M., 2011. Evaluating thermal comfort conditions and health responses during an extremely hot summer in Athens. Build. Environ. 46 (2), 339–344.
Parrish, D.D., Zhu, T., 2009. Clean air for megacities. Science 326, 674–675. https://doi.org/10.1126/science.1176064.
Pérez, G., Coma, J., Sol, S., Cabeza, L.F., 2017. Green facade for energy savings in buildings: the influence of leaf area index and facade orientation on the shadow effect. Appl. Energy 187, 424–437.
Pickett, S.T.A., Cadenasso, M.L., Grove, J.M., Boone, C.G., Groffman, P.M., Irwin, E., Kaushal, S.S., Marshall, V., McGrath, B.P., Nilon, C.H., Pouyat, R.V., Szlavec, K., Troy, A., Warren, P., 2011. Urban ecological systems: scientific foundations and a decade of progress. J. Environ. Manag. 92, 331–362.
Rangel, T.F., Diniz-Filho, A.F., Bini, L.M., 2010. SAM: a comprehensive application for spatial analysis in Macroecology. Ecography 33, 46–50.
Riitters, K.H., O'neill, R.V., Hunsaker, C.T., Wickham, J.D., Yankee, D.H., Timmins, S.P., et al., 1995. A factor analysis of landscape pattern and structure metrics. Landsc. Ecol. 10 (1), 23–39.
Rockström, J., Steffen, W., Noone, K., Persson, Å., Chapin, F.S., Lambin, E.F., et al., 2009. A safe operating space for humanity. Nature 461 (7263), 472–475.
Rosenzweig, C., Solecki, W.D., Parshall, L., Lynn, B., Cox, J., Goldberg, R., et al., 2009. Mitigating New York City's heat island: integrating stakeholder perspectives and scientific evaluation. Bull. Am. Meteorol. Soc. 90 (9), 1297–1312.
Rosenzweig, C., Solecki, W., Hammer, S.A., Mehrotra, S., 2010. Cities lead the way in climate–change action. Nature 467 (7318), 909.
Rybarczyk, G., 2018. Toward a spatial understanding of active transportation potential among a university population. Int. J. Sustain. Transport. 1–12. https://doi.org/10.1080/15568318.2017.1422301.
Santamouris, M., 2013. Using cool pavements as a mitigation strategy to fight urban heat island- A review of the actual developments. Renew. Sustain. Energy Rev. 26, 224–240.
Santamouris, M., 2014. Cooling the cities – a review of reflective and green roof mitigation technologies to fight heat island and improve comfort in urban environments. Sol. Energy 103, 682–703.
Santamouris, M., Cartalis, C., Synnefa, A., Kolokotsa, D., 2015. On the impact of urban heat island and global warming on the power demand and electricity consumption of buildings- A review. Energy Build. 98, 119–124.
Sarrat, C., Lemonsu, A., Masson, V., Guedalia, D., 2006. Impact of urban heat island on regional atmospheric pollution. Atmos. Environ. 40, 1743–1758.
SAS – SAS Institute Incorporated, 2016. JMP™ System for Statistics. Version 13. Released 2016. Cary, NC. USA.
Scheers-Masters, J.R., Schootman, M., Thach, B.T., 2004. Heat stress and sudden infant death syndrome incidence: a United States population epidemiologic study. Pediatrics 113 (6), e586–e592.
Schweitzer, L., Zhou, J., 2010. Neighborhood air quality, respiratory health, and vulnerable populations in compact and sprawled regions. J. Am. Plan. Assoc. 76 (3), 363–371.
Seneviratne, S.I., Donat, M.G., Mueller, B., Alexander, L.V., 2014. No pause in the increase of hot temperature extremes. Nat. Clim. Change 4 (3), 161–163.
Seto, K.C., Güneralp, B., Hutyra, L.R., 2012. Global forecasts of urban expansion to 2030 and direct impacts on biodiversity and carbon pools. Proc. Natl. Acad. Sci. Unit. States Am. 109 (40), 16083–16088.
Seto, K.C., Dhakal, S., Bigio, A., Blanco, H., Delgado, G.C., Dewar, D., Huang, L., Inaba, A., et al., 2014. Chapter 12 - human settlements, infrastructure and spatial planning. In: Climate Change 2014: Mitigation Of Climate Change. IPCC Working Group III Contribution To AR5. Cambridge University Press.
Shaker, R.R., 2015. The well-being of nations: an empirical assessment of sustainable urbanization for Europe. Int. J. Sustain. Dev. World Ecol. 22 (5), 375–387.
Shaker, R.R., Drezner, T.D., 2010. A new technique for predicting the sky-view factor for urban heat island assessment. Geogr. Bull. 51 (2), 85–96.
Shaker, R.R., Ehlinger, T.J., 2014. Exploring non-linear relationships between landscape and aquatic ecological condition in southern Wisconsin: a GWR and ANN Approach. Int. J. Appl. Geospatial Res. (IJAGR) 5 (4), 1–20.
Shaker, R.R., Yakubov, A.D., Nick, S.M., Vennie-Vollrath, E., Ehlinger, T.J., Forsythe, K.W., 2017. Predicting aquatic invasion in Adirondack lakes: a spatial analysis of lake and landscape characteristics. Ecosphere 8 (3). https://doi.org/10.1002/ecs2.1723 e01723.
Sheng, J., Wilson, J.P., Lee, S., 2009. Comparison of land surface temperature (LST) modeled with a spatially-distributed solar radiation model (SRAD) and remote sensing data. Environ. Model. Softw 24 (3), 436–443.
Song, J., Du, S., Feng, X., Guo, L., 2014. The relationships between landscape compositions and land surface temperature: quantifying their resolution sensitivity with spatial regression models. Landsc. Urban Plan. 123, 145–157.
Spokane, A.R., Lombard, J.L., Martinez, F., Mason, C.A., Gorman-Smith, D., Plater-Zyberk, E., et al., 2007. Identifying streetscape features significant to well-being. Architect. Sci. Rev. 50 (3), 234–245.

Stathopoulou, E., Mihalakakou, G., Santamouris, M., Bagiorgas, H.S., 2008. Impact of temperature on tropospheric ozone concentration levels in urban environments. J. Earth Syst. Sci. 117 (3), 227–236.
Stewart, D., Oke, T.R., 2012. Local climate zones for urban temperature studies. Bull. Am. Meteorol. Soc. 93 (12), 1879–1900.
Stocker, T.F., Qin, D., Plattner, G.K., Tignor, M., Allen, S.K., Boschung, J., et al., 2013. *IPCC, 2013: Climate Change 2013: the Physical Science Basis*. Contribution of Working Group I to the Fifth Assessment Report of the Intergovernmental Panel on Climate Change.
Stone, B., 2012. The City and the Coming Climate: Climate Change in the Places We Live. Cambridge University Press, New York, NY.
Synnefa, A., Dandou, A., Santamouris, M., Tombrou, M., Soulakellis, N., 2008. On the use of cool materials as a heat island mitigation strategy. J. Appl. Meteorol. Climatol. 47 (11), 2846–2856.
Szymanowski, M., Kryza, M., 2012. Local regression models for spatial interpolation of urban heat island-an example from Wrocław, SW Poland. Theor. Appl. Climatol. 108 (1–2), 53–71.
Tischendorf, L., Fahrig, L., 2000. On the usage and measurement of landscape connectivity. Oikos 90 (1), 7–19.
Tobler, W.R., 1970. A computer movie simulating urban growth in the Detroit region. Econ. Geogr. 46, 230–240.
Turner, M.G., Gardner, R.H., 2015. Landscape Ecology in Theory and Practice: Pattern and Process, second ed. Springer-Verlag, New York, NY, USA.
Turner, M.G., O'Neill, R.V., Gardner, R.H., Milne, B.T., 1989. Effects of changing spatial scale on the analysis of landscape pattern. Landsc. Ecol. 3 (3–4), 153–162.
UNPD – United Nations Population Division, 2008. World Urbanization Prospects: the 2007 Revision. United Nations Department of Economic and Social Affairs, Population Division, United Nations, New York, 2008. https://esa.un.org/unpd/wup/. (Accessed 25 November 2017).
UNPD – United Nations Population Division, 2014. World Urbanization Prospects: the 2013 Revision. United Nations Department of Economic and Social Affairs, Population Division, United Nations, New York, 2014. https://esa.un.org/unpd/wup/. (Accessed 25 November 2017).
Upmanis, H., 1999. The influence of sky view factor and land-use on city temperatures. In: Upmanis, H. (Ed.), *Influence Of Parks on Local Climate*. Goteborg: Earth Sciences Centre. Goteborg University. A 43, paper 3.
U.S. Census – United States Census Bureau, 2017. 2017 Annual Population Estimates Program. American Factfinder. [cited 2018 May 1] Available at:https://factfinder.census.gov/faces/nav/jsf/pages/community_facts.xhtml#.
Vaz, E., 2016. The future of landscapes and habitats: the regional science contribution to the understanding of geographical space. Habitat Int. 51, 70–78.
Vaz, E., Nijkamp, P., Painho, M., Caetano, M., 2012. A multi-scenario forecast of urban change: a study on urban growth in the Algarve. Landsc. Urban Plan. 104 (2), 201–211.
Voogt, J., 2007. How researchers measure urban heat islands. In: United States Environmental Protection Agency (EPA), State And Local Climate And Energy Program, Heat Island Effect, Urban Heat Island Webcasts And Conference Calls. July, 2007.
Voogt, J.A., Oke, T.R., 2003. Thermal remote sensing of urban climates. Remote Sens. Environ. 86 (3), 370–384.
Wagner, H.H., Fortin, M.J., 2005. Spatial analysis of landscapes: concepts and statistics. Ecology 86, 1975–1987.
Weinzettel, J., Hertwich, E.G., Peters, G.P., Steen-Olsen, K., Galli, A., 2013. Affluence drives the global displacement of land use. Glob. Environ. Chang. 23, 433–438.
Wheeler, D.C., 2014. Geographically weighted regression. In: Handbook Of Regional Science. Springer Berlin Heidelberg, pp. 1435–1459.
Wu, J., 2008. Making the case for landscape ecology: an effective approach to urban sustainability. Landsc. J. 27, 41–50.
Yang, J., Zhi-Hua, W., Kaloush, K.E., 2015. Environmental impacts of reflective materials: is high albedo a 'silver bullet' for mitigating urban heat island? Renew. Sustain. Energy Rev. 47, 830–843.
Zambon, I., Serra, P., Pili, S., Bernardini, V., Ferrara, C., Salvati, L., 2018. A new approach to land-use structure: patch perimeter metrics as a spatial analysis tool. Sustainability 10 (7), 1–17.
Zhou, W., Huang, G., Cadenasso, M.L., 2011. Does spatial configuration matter? Understanding the effects of land cover pattern on land surface temperature in urban landscapes. Landsc. Urban Plan. 102 (1), 54–63.
Zhou, W., Qian, Y., Li, X., Li, W., Han, L., 2014. Relationships between land cover and the surface urban heat island: seasonal variability and effects of spatial and thematic resolution of land cover data on predicting land surface temperatures. Landsc. Ecol. 29 (1), 153–167.
Zhou, W., Wang, J., Cadenasso, M.L., 2017. Effects of the spatial configuration of trees on urban heat mitigation: a comparative study. Remote Sens. Environ. 195, 1–12.